Multiomic ALS signatures highlight sex differences and molecular subclusters and identify the MAPK pathway as therapeutic target

Lucas Caldi Gomes[1*], Sonja Hänzelmann[2,3,4*], Sergio Oller[2,3], Mojan Parvaz[1], Fabian Hausmann[2,3], Robin Khatri[2,3], Melanie Ebbing[2,3], Constantin Holzapfel[2,3], Laura Pasetto[5], Stefano Fabrizio Columbro[5], Serena Scozzari[5], Marie Gebelin[6], Johanna Knöferle[1], Isabell Cordts[1], Antonia F. Demleitner[1], Laura Tzeplaeff[1], Marcus Deschauer[1], Claudia Dufke[7], Marc Sturm[7], Qihui Zhou[8], Pavol Zelina[9], Emma Sudria-Lopez[9], Tobias B. Haack[7,10], Sebastian Streb[11], Magdalena Kuzma-Kozakiewicz[12], Dieter Edbauer[8,13], R. Jeroen Pasterkamp[9], Endre Laczko[11], Hubert Rehrauer[11], Ralph Schlapbach[11], Christine Carapito[6], Valentina Bonetto[5], Stefan Bonn[2,3§], Paul Lingor[1,8,13§,#]

1 Technical University of Munich, School of Medicine, rechts der Isar Hospital, Clinical Department of Neurology, Munich, Germany.
2 Institute of Medical Systems Biology, University Medical Center Hamburg-Eppendorf, Hamburg, Germany.
3 Center for Biomedical AI, University Medical Center Hamburg-Eppendorf, Hamburg, Germany.
4 Department of Medicine, University Medical Center Hamburg-Eppendorf, Hamburg, Germany.
5 Research Center for ALS, Mario Negri Institute for Pharmacological Research, Milan, Italy
6 *Laboratoire de Spectrométrie de Masse Bio-Organique, Université de Strasbourg, Infrastructure Nationale de Protéomique*, Strasbourg, France.
7 Institute of Medical Genetics and Applied Genomics, University of Tübingen, Tübingen, Germany
8 German Center for Neurodegenerative Diseases (DZNE), München, Germany.
9 Department of Translational Neuroscience, University Medical Center Utrecht, Utrecht University, Utrecht, The Netherlands.
10 Center for Rare Diseases, University of Tübingen, Tübingen, Germany.
11 Functional Genomics Center Zürich, ETH Zürich and University of Zürich, Zürich, Switzerland.
12 Department of Neurology, Medical University of Warsaw, Warsaw, Poland.
13 Munich Cluster for Systems Neurology (SyNergy), Munich, Germany.

*,§ These authors contributed equally.

#Corresponding Author: Paul Lingor; email: paul.lingor@tum.de; Clinical Department of Neurology, School of Medicine, rechts der Isar Hospital, Technical University of Munich, Ismaninger Straße 22, 81675 Munich, Germany, Tel.: +498941408257

Abstract

Amyotrophic lateral sclerosis (ALS) is the most common motor neuron disease and lacks effective disease-modifying treatments. Here, we performed a multiomic analysis of the prefrontal cortex of 51 patients with sporadic ALS and 50 control subjects, as well as four transgenic mouse models of C9orf72-, SOD1-, TDP-43-, and FUS-ALS to characterize early and sex-specific disease mechanisms in ALS. Integrated analyses of transcriptomes, (phospho)proteomes, and miRNAomes revealed more pronounced changes in male patients. We identified transcriptome-based human ALS subclusters driven by the immune response, extracellular matrix, mitochondrial respiration, and RNA metabolism. The molecular signatures of human subclusters were reflected in specific mouse models. Individual and integrative multiomics analyses highlighted the mitogen-activated protein kinase pathway as an early disease-relevant mechanism. Its modulation by trametinib in vitro and in vivo validated that mitogen-activated protein kinase kinase 2 is a promising therapeutic target with beneficial effects in female patients.

Main, Introduction

Amyotrophic lateral sclerosis (ALS) is the most common motor neuron disease, largely prevalent in males, and causes paralysis and death within a few years of symptom onset[1]. Most cases are sporadic (sALS), i.e., without a family history, but 10% of cases have a genetic cause (fALS). The most common genetic variants include *C9orf72*, *SOD1*, *TARDBP*, and *FUS* and approximately 10% of patients with sALS carry disease-causing mutations[2]. The etiology of sALS remains unclear, and there are no effective disease-modifying treatments for the disease[3]. An improved understanding of early disease mechanisms could help identify the diagnostic and prognostic biomarkers, thereby uncovering more efficient therapeutic drug targets. Although direct analysis of affected nervous system tissues remains the gold standard in neuropathology, patient samples are only available postmortem and in limited quantities. This increases the risk of describing the end stages of the disease and obscuring mechanisms that occur in earlier phases, which are potentially more favorable drug targets. As in Alzheimer's or Parkinson's disease, ALS is believed to spread over time—from the motor cortex to other cortical brain areas[4–6]. Numerous studies have analyzed the motor cortex in ALS[7–9]. However, as this area is the most severely affected by ALS, it primarily reflects the final stages of the disease[6]. In contrast, the prefrontal cortex (PFC) in Brodmann area 6 typically exhibits only intermediate TDP-43 pathology at the time of death[6], suggesting that analyzing this area could provide insights into earlier disease-mediated alterations.

Previous investigations of ALS brain tissue have primarily focused on individual molecular subsets, including transcripts[7,9,10], miRNAs[11], and proteins[12], suggesting that ALS is a complex and heterogeneous disease. Recent studies have identified potentially distinct ALS populations, which were stratified into different subclusters based on transcriptomics and gene set enrichment analyses (GSEA)[9,13].

In this study, we deciphered early ALS disease mechanisms by profiling the transcriptomes, miRNAomes, and (phospho)proteomes in the PFCs of patients with ALS and four ALS mouse models. We identified strong sex differences and demonstrated that ALS is not a homogeneous disease but consists of different molecular subtypes that are correlated in individual transgenic mouse models of the disease. Multiomic data integration identified several known ALS patho-mechanisms and pathways that have been less prioritized in ALS research to date—particularly the Mitogen-activated protein kinase (MAPK) pathway, which is important for modulating cell survival and differentiation. In vitro and in vivo validation studies underscored MAPK as a putative target for early therapeutic interventions.

Results

Cohort composition and depth of analysis

A deep multiomic characterization of the human postmortem PFC (Brodmann area 6) from 51 patients with neuropathologically confirmed ALS and 50 control (CTR) patients was performed to describe early molecular changes in sALS (Fig. 1a, Table 1, Supplementary Table 1). On average, 19.641 transcripts, 736 miRNAs (mature miRNAs and hairpin precursors), and 2.344 proteins were detected per sample (Supplementary Fig. 1). C9orf72 repeat expansion was detected in one patient with ALS, and another individual carried a pathogenic variant of *NEK1* (c.3107C>G, p.Ser1036Ter)[14] (Supplementary Fig. 2, Supplementary Table 2). For clarity and accuracy, we refer to all cases simply as "ALS". Four transgenic mouse models were analyzed to identify parallels with human ALS. PFCs from presymptomatic or early disease stages were collected from C9orf72-, SOD1-, TDP-43-, or FUS-ALS, with an equal distribution of wild-type and transgenic littermates and sex (n = 20 per model, Fig. 2, Supplementary Fig. 3). In mice, an average of 17.020 transcripts, 842 miRNAs (mature miRNAs and hairpins), 2.568 proteins, and 6.755 phosphosites were detected. Overall, sample quality was high (Supplementary Fig. 4).

Transcriptomic stratification of human ALS into four molecular subclusters

Principal component analysis was performed to assess the effects of disease, sex, and sample origin on the transcriptome, revealing a moderate separation by condition (silhouette score: 0.11 [ALS]; -0.03 [CTR]) but a strong separation by sex (Supplementary Fig. 5). Therefore, we analyzed differentially expressed genes (DEGs) separately for males and females. The number of DEGs was significantly higher in males (72) than in females (2) (Fig. 1b, Supplementary Table 3). Overrepresentation analysis revealed the upregulation of genes involved in *retinoic acid* and *lipid metabolism* in females and downregulation of *extracellular matrix (ECM), collagen,* and *vasculature* in males (Supplementary Fig. 6). Kyoto Encyclopedia of Genes and Genomes (KEGG) pathway analysis showed suppressed *complement/cytokine* and *ECM-receptor signaling* and activation of *oxidative phosphorylation* and *glutamatergic synapse* in males, whereas decreased *complement/coagulation* and activated *ribosomal function* and *oxidative phosphorylation* were found in females (Fig. 1d). Hierarchical clustering of the enriched pathways revealed four distinct clusters: C1–C4. Regulation of *immune response* dichotomized patients with ALS best (C1 and C2 vs. C3 and C4), whereas second-level arborization was mainly driven by *ECM* (C1 vs. C2), *synaptic function*, *RNA splicing,* and *protein folding* (C3 vs. C4, Fig. 1c, Supplementary Table 4). These clusters are reminiscent of previously proposed subtypes[9], where C1 and C2 show similarities to ALS-Oxidative stress (ALS-Ox) (and less to ALS-Retrotransposon reactivated), and C3 and C4 correspond to the ALS-Glial dysfunction (ALS-Glia) subtype (Supplementary Fig. 7). To characterize the clusters using similarly regulated RNA networks, we performed weighted gene co-expression network analysis (WGCNA[15]), resulting in 20 modules (M) (Fig. 1e, Supplementary Fig. 8, Supplementary Table 5). The Mturquoise module was enriched for *mitochondrial respiration* and upregulated in C1 and C2, particularly in males, and driven by neuronal alterations, suggesting increased oxidative respiration in PFC neurons. The Myellow module was enriched for *synaptic function* and showed a similar regulation in C1 an C2. By contrast, the Mtan and Mlightcyan modules were enriched for *immune response,* and *RNA splicing* was upregulated in C3 and C4 (Fig. 1e,f). Molecular subclusters and sex-specific differences drive heterogeneity in the PFCs of patients with ALS.

Finally, transcriptome-based analyses were performed to explore differential alternative splicing (DAS) in the analyzed cohort. TARDBP/TDP-43 and FUS regulate alternative splicing and transcript usage in hundreds of genes[16,17]. TDP-43 also represses cryptic exon splicing

events in *UNC13A*[18]. However, these events are specific to neurons with TDP-43 pathology and are rarely detectable in bulk RNA-Seq at our sequencing depth. The sequences are also not conserved in mice. We identified significant DAS events that occurred more frequently in male patients with ALS than in females (Fig. 3a). DAS was observed in males for *CLTB*, *TPRN*, *NRN1*, and *CAMK2N1* and in females for *TPRN* and the gene encoding TMEM170A-CFDP1, a novel readthrough protein (AC009163.5) (Supplementary Table 6). Genes involved in the regulation of *kinase activity* were particularly enriched in the DAS of male patients with ALS (Supplementary Table 7). Early disease mechanisms appear to be influenced by splicing events, particularly in males. TPRN, a stereocilium-associated protein previously described only in non-syndromic deafness, may play additional roles in the pathogenesis of ALS (Fig. 3d).

Transcriptomes of murine ALS models reflect human ALS subclusters

To explore sex differences in mice, we performed separate differential analyses for male and female mice (Fig. 2, Supplementary Fig. 9). The strongest transcriptomic changes were observed in the C9orf72 mice, reflecting the rapid disease progression observed in this model. Each mouse model was predominantly characterized by the deregulation of specific pathways, that is, *immune/inflammatory response* in C9orf72 mice, *ERK1/2 cascade, development* and *response to* H_2O_2 in SOD1, and *transcription* and *endopeptidase activity* in TDP-43. No enrichment was found in the FUS model (Fig 2a–e, Supplementary Table 8). DAS analyses were also conducted in mice, which showed more balanced results between the sexes (Fig. 3b, Supplementary Fig. 10). We identified *FINB, CPLANE1* (involved in ciliogenesis and migration), and *ATP1B1* (a membrane-bound Na^+/K^+-ATPase) as differentially spliced in male and female models (Fig. 3c), showing enrichment in the terms *translation* and *myelin sheath* (C9orf72), *GTPase activity* and *myelin sheath* (SOD1), *translation* and *heat shock protein binding* (TDP-43), and *purine metabolism* and *basal plasma membrane* (FUS) (Supplementary Table 7).

Next, to assess to which degree the observed alterations in gene expression reflected changes in the cellular composition of the PFC, we estimated the cell-type fractions for the subclusters of human and mouse ALS models using deep learning-based deconvolution[19]. Interestingly, the human subclusters showed changes in the cell fractions that were reflected in the individual mouse models. The SOD1 model and human C1 and C2 groups showed a decrease in glial and endothelial cells and a relative increase in excitatory neurons. The C9orf72 model and human C3 were characterized by a strong increase in glial and endothelial cells and a decrease in excitatory neurons, respectively, suggesting strong neuroinflammation and neuronal loss. The FUS and TDP-43 models showed intermediate levels of glial and neuronal cells (Fig. 2c, Supplementary Fig. 11). Transcriptional changes are partially driven by cell composition. Interestingly, our data suggest that the neurovascular unit in ALS[20] may be affected differently in different subgroups of patients with ALS. Overall, our transcriptomic analyses revealed remarkable similarities between human clusters and mouse models: C1 and C2 showed the best correlation with the SOD1 model, whereas C3 correlated best with the C9orf72 model and, to a lesser extent, TDP-43 and FUS models. Finally, C4 showed a weak correlation with the FUS model (Fig. 2d). While we observed transcriptional and cell composition differences between mouse models and human ALS clusters, we found consistent changes in *MAPK signaling* in the TDP-43, SOD1, and C9orf72 models, as well as human ALS samples (Supplementary Fig.12). Moreover, analysis of the subclusters showed that the classical MAPK pathway was activated in C1 and C2, whereas it was downregulated in C3. Meanwhile, C1 and C2 showed downregulation of the JNK and p38 MAPK pathways, which were activated in C3 (Fig. 2e). Thus, mouse models of ALS reflect the molecular

subgroups of human ALS, which are partially driven by cell fraction changes. The deregulation of MAPK pathways is a common theme in both human ALS and mouse transcriptomes.

Downregulation of hairpin and mature miRNA in males characterize early ALS

To address the role of miRNA-mediated regulation in ALS mechanisms[21], we sequenced small RNAs. Male patients with ALS showed a stronger downregulation of mature miRNAs and miRNA hairpins than female patients (Fig. 3e,f). The higher number of differentially expressed (DE) hairpins compared with the number of mature miRNAs indicates defects in early miRNA biogenesis as a potential early disease mechanism. In males, we observed 17 mature DE miRNAs (15 downregulated, 2 upregulated) and in females, there were 9 DE miRNAs (4 downregulated, 5 upregulated) ($p < 0.1$). For miRNA hairpins, females presented 24 DE hairpins (12 downregulated, 12 upregulated), whereas males presented 99 DE hairpins (86 downregulated, 13 upregulated). The top hits common to males and females included the miRNA hairpins let-7a-3, miR-26a-1, let-7f-1 (all downregulated), and miR-1227 (upregulated) (Fig. 3e–h). Enrichment analysis of the targets of the DE miRNAs revealed pathways involved in *cell growth*, *focal adhesion, integrin binding,* and *kinase activity regulation,* indicating that the ECM/neurovascular unit is an important target of miRNA regulation (Supplementary Fig. 13). Mouse models showed the most pronounced DE of miRNAs in the C9orf72 model (targets annotated for *cell survival/PI3K-Akt, mTOR, MAPK signaling*) followed by the SOD1 model (*cancer* and *lipid metabolism*) (Supplementary Fig. 14, Supplementary Table 9). Among the top five regulated miRNAs, miR-451a was found to be significantly deregulated across all mouse models and human patients with ALS (Fig. 3g,h). Targets of hsa-miR-451a, such as *MAPK1*, *AKT1,* and *BCL2*, are known for their roles in the regulation of cell growth, survival, and apoptosis, whereas other targets, such as *Il6R*, *IKBKB*, and *MIF,* are involved in inflammatory signaling or ECM remodeling, such as *MMP2* and *MMP9* (Fig. 3i, Supplementary Fig. 15). In addition to the pronounced sex-specific regulation of miRNAs, consistent miRNA changes related to the regulation of the MAPK pathway, ECM, and inflammatory signaling were identified and matched the findings of the transcriptomic dataset.

Human proteomic landscape most closely correlates with the TDP-43 model

Subsequently, we assessed the proteomic signatures of early-stage ALS using mass spectrometry. In human samples, we detected 49 (30) differentially expressed proteins (DEPs) in males (females), with annexin A2 (ANXA2) being the only protein downregulated in both sexes ($p < 0.1$). Interestingly, we identified several neurodegeneration-related proteins, such as MATR3, SPART, and SCNA (involved in the genetic forms of ALS, spastic paraplegia, and Parkinson's disease, respectively) (Fig. 4a, Supplementary Table 10). The projection of transcriptomic clusters onto proteomic data did not reproduce subclustering, likely because of the much smaller number of mapped entities (Supplementary Fig. 16). Functional enrichment and unsupervised clustering identified relevant pathways in both sexes, such as *synaptic function*, *immune response*, and *ECM/cytoskeleton*. In contrast, *transmembrane transport, lipid metabolism*, *development*, and *catalytic activity* were enriched in female mice, whereas *cell metabolism* was enriched in male mice (Fig. 4b,c, Supplementary Table 11). In mice, proteomic analyses revealed the strongest changes in the C9orf72 model, where sequestosome 1/p62, a product of the ALS-causing *SQSTM1*[22], showed the strongest upregulation, indicating reduced autophagic flux in a dipeptide accumulation model[23] (Supplementary Figs. 17, 18). pSQSTM1 was also significantly upregulated in the phosphoproteomic analysis (Supplementary Fig. 19). Male SOD1 mice showed one upregulated DEP—exportin-1 (XPO1)—a major regulator of nuclear RNA export. This corresponded to increased *XPO1* expression in this model, which was also observed in TDP-43 females, FUS males, and both sexes in the C9orf72 model (Supplementary Table 3). To

compare Gene Ontology (GO) term enrichment in human and animal proteomics, we used clustering in semantic space[24]. Human proteomics results showed clustering for *differentiation* and *development* (females: clusters 3, 4, 7, and 11; males: cluster 8), *synapse,* and *immune/defense response* (Fig. 4e,f). In contrast, the C9orf72 model showed clustering for *RNA processing, ribosome, translation*, *ATP synthesis*, *development*, *cell adhesion*, *transport*, and *synapse*. Remarkably, the SOD1 model showed strong clustering for *ATP synthesis, mitochondrial respiration*, *translation*, and *vesicle-mediated transport*. Thus, enrichment results underscored the pathways previously identified in the RNA sequencing data. Overall, the human proteome showed the strongest similarity with the TDP-43 model (Fig. 4d). Several mouse models (especially male models) showed increased expression of XPO1—a target in an ALS clinical trial[25] (Supplementary Fig. 20).

Integration of multiomic data reveals sex-specific molecular networks of ALS

After using various omics modalities to identify the molecular pathways associated with early ALS, we employed a biologically motivated approach that focused on identifying valid interaction triplets involving miRNAs, transcripts, and proteins. Triplet miR-769-3p–*ANXA2*–ANXA2 was particularly intriguing because ANXA2 was the only common differentially expressed protein in both sexes (Supplementary Fig. 21, Supplementary Table 12). Valid quadruplets in mouse models, including phosphoproteomic data, highlighted GFAP, SQSTM1, ATXN2L, and XPO1 as salient target proteins (Supplementary Fig. 22, Supplementary Table 12).

Next, we integrated transcriptomic, small RNA, and proteomic data using Multi-Omics Factor Analysis (MOFA)[26]. Because sex was an important differentiating factor (Fig. 4g), MOFA was performed by sex (Fig. 4h, Supplementary Fig. 23). In males, factor 1, mainly driven by hairpin small RNA, explained 23.7% of the variance. Downregulation of hsa-miR-7851, -1285-1, -5096, and a cluster of -1273 isoforms strongly contributed to its weight (Supplementary Fig. 24). MAPK1 plays a central role in the miR-1273 targets (Supplementary Fig. 25). Transcriptome-based factor 3 correlated best with disease condition and was driven by genes responsible for *vesicular function* (*RAB3C, NSF*), *oxidative phosphorylation* (*ND1, ND2*), *cell survival* (*BCL2, BHLHB9*), and *RNA metabolism* (*SNORA73B, RN7SL2*). This factor also contained miR-3648-2, which recruits amyloid precursor protein intracellular domains and regulates survival and neurogenesis[27]. Proteome-dominated factor 4 contains ZO2 and CD44, which are involved in myelination and blood–central nervous system barrier (BCNSB) formation, respectively. Finally, factor 7, which also showed a strong correlation with the disease condition, was dominated by neurofilament heavy, medium, and light polypeptides (NfH, NfM, and NfL, respectively) as well as proteins involved in Ca^{2+}-binding (HPCL4) and ECM formation (PGCA) (Supplementary Fig. 24). In females, factors 1–3 explained 42.6% of the variance, but factors 10 and 12 correlated best with the disease condition (Fig. 4h). Synaptic genes, such as *RAB3C*, *NAPB*, and *SNAP25*, contributed to factor 1 and are upregulated in ALS. The hsa-miR-1285-1, miR-5096, and miR-1273 clusters also contributed to factor 2, similar to factor 1, in males. Factors 3 and 7 (similar to male factor 4) included the oligodendrocyte and myelin markers CD44 and ZO2 (Fig. 4i). Factor 10 contained the antiproteases SERPINA1 and SERPINA3[28] as well as chitinases CHI3L1 and CHI3L2, which are known biomarkers for ALS[29] (Supplementary Fig. 26). Factor 12 downregulated the NFH and MAPK–ERK1/2 regulator PEA15 (Fig. 4j). MOFA analysis underlined the mechanisms identified in the individual omics analyses, such as the downregulation of miRNA clusters (particularly in males, Supplementary Fig. 27), ECM components, and oligodendrocyte and myelin markers. This unbiased data integration strategy highlighted known ALS biomarkers (neurofilaments and chitinases) and the MAPK pathway, especially in females, as important molecular hubs (Fig. 4k).

MAPK pathway emerges as therapeutic target based on multiomic data integration

Single-omics analyses identified several molecular signaling pathways as pharmacological targets that could be more appropriate for different subclusters or sexes of patients with ALS. Currently, licensed drugs target *glutamatergic synapse function* (riluzole), *oxidative stress* (edaravone), *mitochondrial function* (tauroursodeoxycholic acid/phenylbutyrate), or SOD1 itself (tofersen). The major mechanisms revealed in our analysis, such as *immune response* and *ECM/BCNSB function*, have not yet been targeted by licensed drugs. Although multiple molecular pathways identified in our analysis merit therapeutic validation, we decided to focus on the MAPK pathway, which was altered consistently in humans, albeit more pronounced in females and mouse models, across several data types, integration methods, and different subclusters. More specifically, we concentrated on mitogen-activated protein kinase kinase 2 (MAP2K2 or MEK2), as it appeared to be upregulated in the human PFC and multiple mouse models and is central to the female-specific ALS-associated factor 12 (Fig. 4k, Supplementary Fig. 12). Furthermore, MEK2 can be modulated by the clinically approved inhibitor, trametinib[30].

Validation of MEK2 inhibition by trametinib in vitro and in vivo

First, we used primary cortical neuronal cultures from P0–P1 C57BL/6J mice that were treated with glutamate as an in vitro model of excitotoxicity in ALS[31]. Treatment with 5 mM glutamate (six hours) did not affect MEK2 protein expression, but significantly increased pErk1/2 levels. Trametinib attenuates glutamate-induced phosphorylation of Erk1/2. Glutamate treatment also increased cell death (caspase-positive neurons) and reduced the average neurite length, both of which were counteracted by trametinib (Fig. 5a–f, Supplementary Fig. 28). Our data suggest that trametinib attenuates MEK2 activity and reduces Erk1/2 phosphorylation resulting in decreased cell death and increased neurite outgrowth under excitotoxic stress.

To validate the importance of the MAPK pathway in vivo, we selected the SOD1 mouse model, which showed the strongest similarity with the largest human ALS subcluster (C1 and C2) (Fig. 2h). We observed strong MEK2 phosphorylation in the motor neurons of the spinal cord, the main tissue involved in the pathology of this animal model[32] (Fig. 5g,h). In females, pMEK2 levels substantially increased with disease progression, whereas in males, the levels returned to control levels after week 14 (Fig. 5i). We treated SOD1 mice with trametinib for 7 weeks, starting from week 9 (presymptomatic stage), and observed a reduction in ERK1/2 phosphorylation compared with that in vehicle-treated female and male mice (Fig. 5j). Trametinib significantly reduced the autophagy receptor p62 expression in the spinal cord of female but not male mice, correlating with its previously described neuroprotective role of increasing autophagy via transcription factor EB activation[33] (Fig. 5k). p62 also co-localizes with ubiquitin and mutant SOD1 in protein aggregates[34]. Accordingly, we detected a significant reduction in detergent-insoluble SOD1 and ubiquitin in trametinib-treated females but not in males (Fig. 5l,m). Finally, we investigated the effect of trametinib on neurodegeneration. NfL plasma concentration[35] was significantly reduced after trametinib-treatment in female SOD1 mice (Fig. 5n). The striking sex-specific differences in the trametinib treatment response correlated with increased MEK2 phosphorylation during disease progression in female but not male SOD1 mice. Thus, trametinib markedly affects the clearance of protein aggregates, leading to neuroprotection in female SOD1 mice, suggesting that MEK2 is a promising therapeutic target for ALS, particularly in females.

Discussion

In this study, we conducted individual and combined analyses of multiple omics datasets to comprehensively understand the molecular architecture of ALS in the PFC, an area affected in the later stages by TDP-43 pathology and that has the potential to reveal early disease mechanisms[6]. We observed that significant sex-specific differences are often more pronounced in males, which is aligned with the higher prevalence of ALS in males[1]. Previous studies have also identified sex-specific differences in the blood of patients with ALS[36,37] as well as therapeutic responses in ALS mouse models[38,39]. However, current therapeutic options, clinical trials, and Food and Drug Administration guidelines for clinical trial design[40] do not consider patient sex in differential therapy. Our data, especially the sex-specific differences in MAPK signaling and therapeutic tractability, argue for a stronger consideration of sex as a covariate in ALS clinical trials.

Phenotypic heterogeneity is clearly recognized in ALS[41], as reflected by stratification in onset or disease progression rate, and previous transcriptomic analyses have suggested molecular subtypes[13]. We identified four clusters in our human ALS cohort based on the transcriptome, partially mirroring previously identified ALS-Ox, ALS-Glia, and ALS-Transposable elements subtypes[9]. While the ALS-Glia and ALS-Ox clusters correlated with clusters C1 and C2 and C3 and C4, respectively, the ALS-TE cluster was only marginally represented in our data. As we analyzed the PFC, an area wherein TDP-43 aggregation is observed later than that in the motor cortex, our data reinforce that ALS-TE is driven by TDP-43 dysfunction[9]. Moreover, this suggests that molecular subtypes of ALS may evolve with time and are subject to changes during the disease course. Thus, exploring liquid biomarkers could aid in patient stratification and personalized clinical trials.

Furthermore, we suggest that the molecular phenotype in the four analyzed mouse models can be approximated to these subtypes, making these models potential surrogates for the molecular subgroups in humans. Notably, the oldest and most frequently used model, the SOD1.G93A mouse, correlated best with the largest clusters C1 and C2. Although not representative of all human ALS cases, our findings indicate that this model represents an important subgroup of the disease based on the identified dysregulated pathways.

Integrated analysis of multiomic datasets has identified several dysregulated pathways relevant for ALS, including mitochondrial respiration/oxidative stress, transcriptional regulation/splicing, and protein misfolding[3]. Additionally, previously less prioritized pathways—including the dysregulation of the ECM and BCNSB or the MAPK pathway—were identified. The deregulation of pathways that are only distantly related suggests the need for combinatorial drug therapies to address ALS mechanistically. Remarkably, we found evidence of female-predominant deregulation of the MAPK pathway in integrative analyses, but it did not contribute to the separation of clusters C1–C4. Therefore, the MAPK pathway may be an interesting therapeutic target for all human ALS subgroups. MAPKs are fundamental signal transducers that are involved in cell proliferation, differentiation, survival, and death[42]. Extracellular and intracellular signals are integrated by MAPK, and the overactivation of MAPK signaling, for example, via the abnormal phosphorylation of ERK1/2, has been reported in human and ALS mouse models[43]. A Ser/Thr kinase belonging to the MAPK superfamily—the MAPK/MAK/MRK [MOK] kinase—has also been linked to impaired microglial function and inflammatory insults associated with ALS pathophysiology[44]. Increased phosphorylation of ERK1/2 was also observed in our glutamate toxicity model, and pMEK2 expression was increased in the SOD1 mouse model, reproducing the aberrant activation of this pathway that was restored by the MEK2-inhibitor trametinib. However, this effect was most pronounced in females, suggesting a sex-specific efficacy. Notably, our experimental approach did not target neurons exclusively. Nevertheless, our primary cultures mainly contained neurons (~95%), and all staining procedures for both in vivo and in vitro experiments focused on neurons. While

391 other cell types may be involved, the evidence presented here supports the significance of the
392 MEK2–MAPK pathway in neurons.
393 Currently, one phase I/II clinical trial is examining the safety, tolerability, and efficacy of
394 trametinib in patients with ALS (clinicaltrials.gov identifier:NCT04326283). Our data support
395 the independent evaluation of male and female patients and suggest that the ECM, immune
396 response, and RNA processing machinery are potential targets for therapeutic intervention
397 that need further exploration.
398 Despite the limitations of our study (e.g., the retrospective view permitted by postmortem
399 tissue analysis and restricted balancing of sex and disease stage due to the limited number of
400 well-characterized postmortem brain samples), we aimed to provide valuable insights into the
401 molecular architecture of ALS. While analyzing over 100 brain samples helped identify
402 molecular subclusters, a larger sample size may provide a more detailed view of the
403 subgroups. Nevertheless, analyzing the PFC tissue allowed us to study the earlier stages of
404 the disease, offering a unique perspective compared with those of previous studies. Our robust
405 multiomic, computational, and integrative approaches identified subclusters that are
406 reminiscent of previously identified subtypes, yet show clear differences. Additionally, we
407 emphasize the role of splicing and transcript usage in early disease regulation, involving
408 several ALS-related genes. Overall, our study contributes towards unraveling the complexity
409 of ALS and lays the groundwork for further research in the field.
410 Our study also compared human brain tissue with samples from transgenic mouse models of
411 ALS. Although clear correlations were found between mouse models and molecular subtypes
412 of sALS, the four analyzed models represent specific scenarios. Other models for each of the
413 four studied genes could potentially yield different results[45]. Furthermore, we did not analyze
414 DNA methylation status or other post-translational modifications (such as glycation,
415 methylation, or acetylation) that could provide further insights into ALS-specific dysregulation,
416 as much as a single cell-based analysis could yield an additional layer of detail.
417 In this comprehensive integration of human tissue- and animal model-derived multiomic data,
418 we emphasized sex-specific differences in ALS pathology, identified molecular clusters, and
419 highlighted their importance for clinical trials and the development of novel therapeutic
420 strategies. The validation of omics results relies on multiple systems, as each mouse model
421 system only reproduces parts of the human pathology. Our data suggest the need for the
422 validation of additional molecules and pathways and justify the further exploration of the MAPK
423 pathway as therapeutic ALS treatment targets.
424
425

Methods

Human postmortem PFC samples

Human PFC samples were provided by four different brain banks: The Netherlands Brain Bank, King's College London Brain Bank (London Neurodegenerative Diseases Brain Bank), Parkinson's UK Brain Bank, and the Oxford Brain Bank. In total, 51 ALS and 50 CTR samples (without any signs of neurodegeneration) were included. Frozen tissues were shipped on dry ice to the rechts der Isar Hospital Department of Neurology at the Technical University of Munich and stored at -80 °C (Supplementary Table 1). Ethical approval for the use of human tissues was obtained from the Ethics Committees of the University Medical Center Göttingen (2/8/18 AN) and the Technical University Munich (145/19 S-SR). For sampling, PFC samples were transferred to a cryostat chamber at -20 °C and punched with a 20-G Quincke Spinal Needle (Becton Dickinson, Franklin Lakes, NJ, USA). Subsequently, ∼20 mg tissue was collected in RNAse-/DNAse-free tubes and stored at -80 °C until further use.

ALS animal models

Four transgenic mouse models representing the most frequent ALS-causing genes were used for the multiomic studies. Animal handling and experiments in this study were performed in accordance with the applicable animal welfare laws and approved by the respective regulatory organs of the involved research centers. The animals were kept in standard cages in a pathogen-free facility under a 12-hour light/dark cycle. The mice were provided with unrestricted access to food and water. B6;129S6-Gt(ROSA)26Sortm1(TARDBP*M337V/Ypet)Tlbt/J mice[46] (here simply referred to as TDP-43 mice) were provided by the Department of Translational Neuroscience of the University Medical Center Utrecht. This model was generated by inserting an 80 kb genomic fragment carrying the human TDP-43 locus (including a patient-derived M337V mutation). TDP-43 transgenic and control wild-type mice were euthanized at the age of 26 weeks (presymptomatic stage) for biomaterial collection. B6SJL-Tg(SOD1*G93A)1Gur/J mice[32] (here referred to as SOD1 mice) were provided by the Laboratory of Translational Biomarkers, Mario Negri Institute for Pharmacological Research, Milan. High-copy number B6 congenic Tg(SOD1*G93A)1Gur/J SOD1*G93A male mice from The Jackson Laboratory (Bar Harbor, ME, USA) were bred with C57BL/6 female mice to obtain non-transgenic and mutant transgenic G93A*SOD1-expressing mice. SOD1 transgenic and control animals were sacrificed 14 weeks after birth (presymptomatic stage). (Poly)GA-NES/C9orf72(R26(CAG-Isl-175GA)-29 × Nes-Cre) mice[47] (here referred to as C9orf72 mice) were provided by the German Center for Neurodegenerative Diseases in Munich. To generate transgenic animals, plasmids were electroporated to enable the conditional expression of dipeptide-repeat proteins (DPRs). DPRs were created by inserting 175 GFP-(GA) genes encoded by non-repeating alternate codons downstream of a floxed stop cassette in the pEX CAG stop-bpA vector. Electroporation was performed on murine recombination-mediated cassette exchange embryonic stem cells at the Rosa26 safe harbor locus. Mouse lines with germline transmission, known as GAstop, were obtained and subsequently backcrossed to a C57BL/6N background until a confirmed purity of over 98% was achieved (using SNP genotyping). C9orf72 transgenic and control animals were sacrificed 4.5 weeks after birth (early symptomatic stage). Tg (Prnp-FUS)WT3Cshw/J mice[48] (hereafter referred to as FUS mice) were provided by the Laboratory of Translational Biomarkers, Mario Negri Institute for Pharmacological Research, and were sacrificed four weeks after birth. For each model, ten transgenic and ten non-transgenic mice were selected and balanced for sex.

Preparation of PFC from ALS mouse models

The mice were perfused with 50 mL of ice-cold phosphate-buffered saline (PBS) prior to microdissection. The head was removed by cutting the base of the skull followed by skin removal. The skull was removed using small incisions followed by microdissection of the PFC in both hemispheres. The olfactory bulb and cerebellum were removed by cutting the cerebellar peduncle starting from the olfactory bulb and continuing along the interhemispheric fissure using tweezers with fine tips. The cortex was removed from the rest of the brain. Incisions were made in the middle of the cortex to excise the PFC (Supplementary Fig. 29). Freshly prepared PFCs were collected in nuclease-free tubes and stored at -80 °C until RNA and protein isolation experiments were performed.

RNA and DNA isolation from human and mouse tissue samples

Total RNA was isolated from human and animal PFC samples using TRIzol Reagent (Sigma-Aldrich, Taufkirchen, Germany). To ensure proper handling of the RNA, all related experiments were conducted in an RNA workstation fume hood. In brief, 500 µL TRIzol was added to each sample, and the tissues were homogenized using a plastic homogenizer. Subsequently, 50 µL of 1-bromo-3-chloro-propane (Sigma-Aldrich) was added. The reaction tubes were inverted for 10–15 s and incubated at room temperature (22–25°C) for three minutes. The resulting lysates were centrifuged at 12 000 × *g* for 15 min at 4 °C, leading to phase separation. The RNA-containing aqueous phase was carefully collected and transferred to a fresh nuclease-free tube. To precipitate the RNA, 250 µL of 2-propanol (AppliChem, Darmstadt, Germany) and 2 µL of GlycoBlue Coprecipitant (15 mg/mL) (Thermo Fisher Scientific, Waltham, MA, USA) were added to each sample. The mixture was thoroughly vortexed and incubated overnight at -20 °C. Samples were centrifuged at 12 000 × *g* for 30 min at 4 °C the following day. The supernatant was discarded, and the RNA pellets were washed three times with 75% ice-cold ethanol (AppliChem). After air-drying the pellets for a few minutes under a fume hood, they were reconstituted with 15–20 µL nuclease-free water (Sigma-Aldrich). The reconstituted RNA was completely dissolved by incubation at 55 °C for two minutes in a thermoshaker. Following RNA isolation, DNase treatment was performed to eliminate DNA contamination. For this purpose, 5 µL 10× DNAse I Incubation Buffer (Life Technologies, Carlsbad, CA, United States), 5 µL DNase I (2 U/µL), and 0.5 µL RNaseOUT (40 U/µL) were added to each sample. Nuclease-free water was added to a final volume of 50 µL, and the samples were then incubated at 37 °C for 20 min. Finally, the RNA samples were purified and concentrated using an RNA Clean & Concentrator-5 Kit (Zymo Research, Irvine, CA, USA) following the manufacturer's instructions. A QIAamp DNA Mini Kit (Qiagen, Hilden, Germany) was used for DNA isolation from human midbrain samples according to the manufacturer's instructions. After RNA and DNA isolation, the concentration and purity of nucleic acids were assessed using a NanoDrop One spectrophotometer (Thermo Fisher Scientific). RNA integrity was evaluated using an Agilent 6000 NanoKit on a 2100 Bioanalyzer (Agilent, Santa Clara, CA, USA).

DNA sequencing experiments and C9orf72 repeat expansion analysis

Prior to the DNA sequencing experiments, the quality of the isolated DNA was determined using a 4200 TapeStation System (Agilent). The AmpliSeq protocol (Illumina, San Diego, CA, USA) was used in subsequent steps. We used a target panel of 566 amplicons covering 30 ALS-related genes: *TARDBP, DCTN1, ALS2, ERBB4, TUBA4A, CHMP2B, NEK1, MATR3, SQSTM1, FIG4, C9orf72, SIGMAR1, VCP, GLE1, SETX, OPTN, HNRNPA1, KIF5A, TBK1, ANG, SPG11, CCNF, FUS, PFN1, MAPT, VAPB, SOD1, CHCHD10, NEFH,* and *UBQLN2.* Using this panel, DNA samples (50–100 ng) were amplified over 14 PCR cycles. The amplicons were digested, and AmpliSeq combinatorial dual indices were ligated for multiplexing. The quality and quantity of the enriched libraries were validated using a 4200

TapeStation System (Agilent). The average fragment size of the amplified product was 480 bp. The libraries were standardized to a concentration of 9 nM in Tris–Cl (10 mM, pH 8.5) supplemented with 0.1% Tween 20. Cluster generation and sequencing were performed using the MiSeq platform (Illumina) following the standard protocol. The loading concentration was 9 pM, and 15% phiX was added. The sequencing configuration was a 250-bp paired-end sequencing. C9orf72 repeat expansion analysis was performed using the AmplideX PCR/CE C9orf72 Kit (Asuragen, Austin, TX, USA). Briefly, DNA samples (n = 51, 40 ng each) were amplified using the three-primer GGGCC-repeat-primed configuration (combining flanking primers and a GGGCC-repeat-specific primer). This configuration allows the sizing of GGGCC alleles of up to 145 repeats and simultaneous detection of expanded GGGCC alleles with > 145 repeats. The PCR conditions consisted of initial denaturation (five minutes, 98 °C), 37 cycles (35 s, 97 °C; 35 s, 62 °C; and 3 min, 72 °C), and final elongation (10 min, 72 °C). Capillary electrophoresis was carried out on an ABI 3730 DNA Analyzer (Applied Biosystems, Waltham, MA. USA) using a ROX 1000 Size Ladder (Asuragen), followed by analysis with GeneMapper 4.0 software (Applied Biosystems) and conversion of peak size to GGGGCC repeat length via the calibration curve method according to the manufacturer's instructions.

Preparation of RNA libraries for sequencing experiments

The mRNA and small RNA sequencing experiments were conducted at the Functional Genomics Center, Zürich. For mRNA sequencing, two different library preparation kits were used: the TruSeq Stranded mRNA Kit (Illumina; short read sequencing) and the SMARTer Stranded Total RNA-Seq Kit v2 Pico Input Mammalian (Takara Bio USA, San Jose, CA, USA; short read sequencing). In the TruSeq protocol, total RNA samples (100–1000 ng) were subjected to poly-A enrichment and reverse transcription to generate double-stranded cDNA. The cDNA was fragmented, end-repaired, adenylated, and ligated to TruSeq adapters containing unique dual indices for multiplexing. Fragments with adapters at both ends were selectively enriched using PCR amplification, resulting in a smear with an average fragment size of ∼260 bp. The libraries were subsequently normalized to 10 nM in Tris–Cl (10 mM, pH 8.5) containing 0.1% Tween 20. For the SMARTer Stranded Total RNA-Seq Kit protocol, total RNA samples (0.25–10 ng) were reverse-transcribed using random priming into double-stranded cDNA in the presence of a template switch oligo (TSO). The generated cDNA fragments contained sequences derived from random priming oligos and the TSO. PCR amplification with primers binding to these sequences incorporated full-length Illumina adapters, including a multiplexing index. The ribosomal cDNA was cleaved using ZapR in the presence of mammalian R-Probes. The remaining fragments were enriched through a second round of PCR amplification using primers designed to match the Illumina adapters, resulting in a smear with an average fragment size of ∼360 bp. The libraries were normalized to 5 nM in Tris–Cl (10 mM, pH 8.5) containing 0.1% Tween 20. To validate the quality and quantity of the isolated RNA and enriched libraries, an Agilent Fragment Analyzer was used for the TruSeq kit, while the 4200 TapeStation System (Agilent) was used for the SMARTer Kit.

RNA sequencing

Sequencing was performed using the Illumina platforms NovaSeq 6000 (for transcriptomics) and HiSeq 2500 (for small RNA sequencing) according to standard protocols. Small RNA sequencing was performed using RealSeq-AC miRNA (SomaGenics, Santa Cruz, CA, USA) (short read sequencing). All samples were quantified and quality was controlled using an Agilent Fragment Analyzer. Briefly, RNA samples (1 ng–1 ug) were adaptor-ligated, circularized, and reverse-transcribed into cDNA. The cDNA samples were amplified using PCR, which also incorporated sample barcodes. The library product, a peak with a fragment size of ∼149 bp, was normalized to 10nM in Tris–Cl (2 mM, pH 8.5) containing 0.1% Tween

20. The quality and quantity of the enriched libraries were validated using an Agilent Fragment Analyzer. Transcriptomics data were processed using the Nextflow Core RNASeq pipeline version 3.0[49]. The data were demultiplexed with bcl2fastq, and the fastq files underwent several quality checks, including FastQC[50]. Salmon[51] was used for pseudoalignment and quantitation with a Salmon index built using GRCm39 with annotations from GENCODE vM26 for mouse data and GRCh38 with annotations from GENCODE v37 for human data. Count matrices from Salmon were used for the downstream analyses (Supplementary Table 13). The count matrices were filtered, retaining genes with at least ten counts in 50% of the samples for any condition or sex. We used the clusterProfiler R package[52] and GO biological processes and molecular functions for GSEA, filtering terms by size between 10 and 500 genes and correcting for multiple testing (Benjamini–Hochberg correction).

Global proteomics of mouse and human PFC tissue samples

Tissues from both human PFCs and four different mouse models were prepared. The tissues were ground with a biomasher using 350 µL MeOH:H_2O (4:1). Protein pellets were resuspended in 200 µL Laemmli buffer (10% SDS, 1 M Tris pH 6.8, and glycerol) and then centrifuged at 16.600 x g at 4 °C for five minutes. The protein concentration was determined using a DC assay (Bio-Rad, Hercules, CA, USA) following the manufacturer's instructions. Each sample, containing 100 µg protein lysate, was heated at 95 °C for five minutes and loaded onto a 5% acrylamide SDS–PAGE stacking gel (prepared in-house). Prior to overnight digestion at 37 °C using modified porcine trypsin (Mass Spectrometry Grade, Promega, Madison, WI, USA) at an enzyme–protein ratio of 1:80, the gel bands were reduced and alkylated. The resulting peptides were extracted using 60% acetonitrile (ACN) followed by 100% ACN. The peptides were resuspended in 30 µL H_20, 2% ACN, and 0.1% fluoroacetic acid. iRT peptides (Biognosys, Schlieren, Switzerland) were added to each sample as an internal quality control (QC). NanoLC–MS/MS analyses were conducted using a nanoAcquity UltraPerformance LC (UPLC) system (Waters, Milford, MA, USA) coupled to a Q-Exactive Plus Mass Spectrometer (Thermo Fisher Scientific). The solvent system consisted of 0.1% formic acid (FA) in water (solvent A) and 0.1% FA in ACN (solvent B). Samples equivalent to 800 ng protein were loaded onto a Symmetry C18 precolumn (20 mm × 180 µm with 5 µm diameter particles, Waters) over three minutes at a flow rate of 5 µL/min with 99% solvent A and 1% solvent B. Peptides were separated on an ACQUITY UPLC BEH130 C18 column (250 mm × 75 µm with 1.7 µm diameter particles) at a flow rate of 400 nL/min. The following gradient of solvent B was used: 1–8% over 2 min, 8–35% over 77 min, 35–90% over 1 min, 90% for 5 min, and 90–1% over 2 min. Samples from each cohort were injected in a random order. The system was operated in data-dependent acquisition (DDA) mode, automatically switching between MS (mass range 300–1800 *m/z* with R = 70 000, automatic gain control [AGC] fixed at 3.10^6 ions, and the maximum injection time set to 50 ms) and MS/MS (mass range 200–2000 *m/z* with R = 17 500, AGC fixed at 1.10^5, and the maximum injection time set to 100 ms) modes. The ten most abundant precursor ions were selected on each MS spectrum for further isolation and higher energy collisional dissociation, excluding monocharged and unassigned ions. The dynamic exclusion time was set to 60 s. A sample pool was injected as an external QC every six samples for the human cohort and every five samples for the mouse cohort. MaxQuant[53] version 1.6.14 was used to process raw data. The Andromeda[54] search engine was used to assign peaks with trypsin/P specificity against a protein sequence database generated in-house containing all human (20 421 entries as of August 24, 2020) or mouse entries (17 134 entries for SOD1 and TDP-43 models as of March 27, 2020, and 17 061 entries for C9orf72 and FUS models as of September 29, 2020) extracted from UniProtKB/Swiss-Prot. Methionine oxidation/acetylation of the protein N-termini was used as a variable modification, whereas cysteine carbamidomethylation was used as a fixed modification. The

"match between runs" option was enabled to facilitate protein quantification. To control false discoveries, a maximum false discovery rate of 1% was implemented (at both peptide and protein levels), employing a decoy strategy. Intensities were extracted from the Proteingroup.txt file for statistical analyses. The MaxQuant protein vs. sample table was used for downstream analyses, including label-free quantitation intensities. Only Swiss-Prot proteins were retained, whereas TrEMBL proteins were removed for higher reliability. After filtering out low abundant proteins, i.e., proteins that were detected in less than 50% of the samples in any combination of condition and sex, and imputing missing values using the missForest[55] algorithm, the intensities were log2-transformed and used for principal component exploration, constructing heat maps, and differential abundance analysis. The limma package[56] was used for linear modeling, and *p*-values were adjusted using the Benjamini–Hochberg correction. The protein names were mapped to the corresponding genes and used to search for enriched biological processes and molecular functions using the criteria described in the transcriptomics data processing, with a $p < 0.01$ threshold for functional annotation analyses.

Phosphoproteomics on mouse PFC brain tissue samples

Starting with the protein extracts from the global proteomics experiments, protease inhibitors (Sigma-Aldrich, P8340) and phosphatase inhibitors (final concentration in Na_3VO_4 = 1 mM) were added to samples. Protein concentration was determined using the RC DC Protein Assay (Bio-Rad) according to the manufacturer's instructions. Proteins for each sample (250 µg) were reduced and alkylated prior to an in-house optimized single-pot, solid-phase-enhanced sample preparation protocol (adapted from Hughes et al., Nat Protoc, 2019). Briefly, beads A (Sera-Mag SpeedBeads, Fisher Scientific, Schwerte, Germany, 45152105050250) and B (Sera-Mag SpeedBeads, Fisher Scientific, 65152105050250) were combined (1:1) and, after three washing steps with H_2O, were added to the samples (bead–protein ratio of 10:1 for each type of bead, meaning a 20:1 ratio for the combination of beads). After inducing protein binding to the beads with 100% ACN for 18 min, the bead and protein mixtures were washed twice with 80% ethyl alcohol and once with 100% ACN before being resuspended in 95 µL NH_4HCO_3 prior to overnight on-bead digestion (enzyme–protein ratio of 1:20) at 1 000 rpm at 37 °C using modified porcine trypsin/Lys-C Mix (Mass Spectrometry Grade, Promega). The digestion was stopped using trifluoroacetic acid (TFA) (final pH < 2). The recovered peptides were resuspended in 170 µL 80% ACN and 0.1% TFA, and MS PhosphoMix I Light (Sigma-Aldrich) was added to each sample (peptide [µg]–mix [fmol] ratio of 1:6). Phosphopeptide enrichment was performed on 5 µL phase Fe(III)–NTA cartridges on an AssayMAP Bravo platform (Agilent) following the immobilized metal affinity chromatography protocol. Briefly, cartridges were washed and primed with 50% ACN, 0.1% TFA and then equilibrated with 80% ACN, 0.1% TFA. Subsequently, 100-µL samples were loaded onto the phase at a rate of 2 µL/min and then washed with 80% ACN, 0.1% TFA before being eluted in 20 µL 1% NH_4OH at 5 µL/min. After enrichment, FA and MS PhosphoMix I Heavy (Sigma-Aldrich) (peptide [µg]–mix [fmol] ratio of 1:6) were added to each sample. Dried phosphopeptides were resuspended in 40 µL H_2O, 2% ACN, 0.1% FA. Sample preparation steps for the C9orf72 and FUS mouse models were identical to those previously described for SOD1 and TDP-43, except that proteins were extracted from new tissue samples immediately before the phosphoproteomics experiment.

NanoLC–MS/MS analyses were conducted using a nanoAcquity UPLC system (Waters) coupled with a Q-Exactive HF-X Mass Spectrometer (Thermo Scientific) equipped with a Nanospray Flex ion source. The solvent system consisted of 0.1% FA in water (solvent A) and 0.1% FA in ACN (solvent B). Samples were loaded onto an ACQUITY UPLC Peptide BEH C18 Column (250 mm x 75 µm, 1.7 µm diameter particles) over three minutes at a flow rate

of 5 µL/min with 99% solvent A and 1% solvent B. Phosphopeptides were separated on an ACQUITY UPLC M-Class Symmetry C18 Trap Column (20 mm x 180 µm, 5 µm diameter particles; Waters) at a flow rate of 400 nL/min using a gradient of solvent B as follows: 1–2% over 2 min, 2–35% over 77 min, and finally 35–90% over 1 min. The samples in each group were injected in random order. The instrument was operated in DDA mode with automatic switching between the MS and MS/MS modes. MS scans were performed in the mass range of 375–1500 *m/z* with R = 120 000, an AGC fixed at 3.106 ions, and a maximum injection time of 60 ms. MS/MS scans were conducted in the mass range of 200–2000 *m/z* with R = 15 000, an AGC fixed at 1.105 ions, and a maximum injection time of 60 ms. In each MS spectrum, the ten most abundant ions were selected for further isolation and higher-energy collisional dissociation, excluding monocharged and unassigned ions. A dynamic exclusion time of 40 s was used to prevent the reanalysis of previously selected ions. The obtained raw phosphoproteomics data were processed using MaxQuant version 1.6.14. Peaks were assigned using the Andromeda search engine with trypsin/P specificity against an in-house-generated protein sequence database containing mouse entries from UniProtKB/Swiss-Prot (17 061 entries as of September 29, 2020). The peptides were required to have a minimum length of seven amino acids, and a maximum of one missed cleavage was allowed. These modifications include methionine oxidation, acetylation of protein N-termini, and phosphorylation of serine, threonine, and tyrosine. Cysteine carbamidomethylation was used as a fixed modification. Protein quantification utilized the “match between runs” option. A maximum false discovery rate of 1% (at both peptide and protein levels) was implemented using a decoy strategy. The intensities were extracted from the Phospho (STY).txt file and processed using the Perseus platform[57] version 2.0.7.0, during which contaminants and reversed proteins, as well as proteins with negative scores, were removed. Using the “expand sites table” option, the intensities of the different phosphopeptides involved in one phosphosite were summed, and phosphosites with a localization probability below 75% were removed. The Perseus output table was used for statistical analyses.

Only proteins that were detected in more than 50% of the mouse samples of any combination of sex and condition were retained for each dataset. The intensities were log2-transformed, quantile normalization was applied, and missing values were imputed to the lowest quartile. The remaining data processing for phosphoproteomics followed the procedure described above for proteomics data processing.

Small RNA sequencing data-processing and miRNA target prediction

Small RNA data were processed using the Nextflow Core smRNASeq pipeline version 1.0[49]. Reads were trimmed and aligned against miRBase[58] version 22.1 using Bowtie1[59], both for mature miRNAs and hairpins. miRNAs with at least ten counts in 50% of the samples of any condition and sex were retained, and the rest were filtered out. Unnormalized count matrices were used for subsequent DESeq2[60] differential expression analysis after stratifying by sex and adjusting for *p*-values using the Benjamini–Hochberg correction. Mature miRNAs were mapped to their corresponding genes using miRDB version 6.0[61], excluding matches with scores < 60 or > 800 targets, as recommended. For each miRNA present in the miRNA expression matrices, we obtained experimentally validated targets from miRTarBase[62] 8.0 and predicted targets from miRDB miRBase version 22[61]. miRTarBase[62] provides the most extensive curated database of validated miRNA–target interactions (MTI) collected from literature using natural language processing to select functional miRNA studies. Additionally, the miRDB database includes MTIs predicted by MirTarget, which uses a support vector machine (SVM) to analyze thousands of high-throughput sequencing experiments[63]. Each experiment is assigned a probability score, which serves as the SVM's output. A higher probability score indicates a higher likelihood of accurate target prediction. Therefore, we set

a threshold of 0.6 on the output probabilities to select only highly likely MTIs. Finally, we joined the miRNA–target pairs from both sources for further analysis.

Cell-type deconvolution analyses

Single-cell reference-based cell-type deconvolution of RNA-Seq in mouse models was performed using Scaden[19]. We used healthy adult scRNA-Seq datasets for mouse[64] and human[65]. Scaden uses a fully connected deep neural network ensemble trained on pseudo-bulks simulated from reference scRNA-Seq data. Before deconvolution, we filtered the scRNA-seq data using Scanpy[66] to maintain at least 200 genes expressed per cell and at least five cells expressing one gene. For Scaden, counts per million (CPM) of simulated pseudo-bulks and transcripts per million (TPMs) of the data to be deconvolved were used. In this study, CPM was used for scRNA-Seq instead of TPMs because scRNA-Seq consists of unique molecular identifier counts and does not include gene-length bias. We used a variance cutoff of 0.01, and the mean squared error was calculated for each batch as loss.

Differential Alternative Splicing analysis

The splicing tool SUPPA2 version 2.3 was used to analyze DAS for seven alternative splicing events: exon skipping, mutually exclusive exons, intron retention, alternative 3'-splice site, alternative 5'-splice site, alternative first exon, and alternative last exon. SUPPA2 was used with multipleFieldSelection() to select the TPM values of the transcripts, followed by GenerateEvents with the parameters -f ioe -e SE SS MX RI FL and annotation files GENCODE v37 for human data and GENCODE vM26 for mouse data. The inclusion values (PSupplementary) were calculated using psiPerEvent, and the differences in PSupplementary (ΔPSupplementary) between the mutant and control conditions were determined using diffSplice with parameters -m empirical -l 0.05 -gc –save tpm_events to detect anomalies in the splicing landscape.

Multi-Omics Factor Analysis

We used MOFA 2 version 1.4.0 to integrate data from multiple omics levels for the human cohort, including transcriptomics, miRNA, and proteomics. The MOFA model was trained on the data, and downstream analyses were performed. Each omics type was preprocessed in its own manner, and the default training parameters were used. The MOFA models were initialized with 15 initial factors, and convergence was reached when the evidence lower bound (ELBO) value did not change with more than a deltaELBO value of 1e-4%.

Gene ontology, pathway enrichment analyses, and protein interaction networks

GSEA was performed using gseGO and gseKEGG from the clusterProfiler R package, with biological processes and molecular functions chosen as background databases for GO enrichment. The *p*-value cutoff was set at 0.05. Differential expression was presented using volcano plots generated with the Enhanced Volcano plot package in R, and over-representation analysis was performed on genes that showed at least one significant DAS event using the clusterProfiler function enrichGO, with a *p*-value cutoff of 0.1 and Benjamini–Hochberg correction for multiple hypothesis testing. Protein–protein interaction networks were created using the STRING protein interaction network database version 11.0[67,68] using standard settings.

Weighted Correlation Network Analysis

To conduct a weighted gene co-expression analysis, we employed the WGCNA package[15]. Pairwise Pearson correlations were calculated to establish signed regulatory networks within the WGCNA. By constructing an adjacency matrix, we applied a soft-thresholding technique

to approximate a scale-free topological network. Eigengenes or eigenproteins were calculated as the first principal components of each module. This resulted in the development of several modules. We merged similar modules based on hierarchical clustering (SOD1: 0.4, C9orf72: 0.4, FUS: 0.5, TDP-43: 0.4 for RNA-Seq and 0.25 for proteomics). We calculated the relationships between WGCNA modules and traits. Sex was also included in the traits resulting in four traits: male ALS, female ALS, male CTR, and female CTR. First, we filtered modules based on the significance of the module–gene relationship ($p < 0.05$) and then selected modules that were highly correlated with either male or female ALS. The correlation cutoffs differed between the mouse models (SOD1: 0.5, C9orf72: 0.3, FUS: 0.3, and TDP-43: 0.5 for RNA-Seq and SOD1: 0, C9orf72: 0, FUS: 0, and TDP-43: 0 for proteomics). Using WGCNA, we also analyzed co-expression networks in mouse models. The minimal module size was set to 30 with a merge height of 0.4–0.5 and a correlation threshold of 0.3–0.5 (Supplementary Table 14).

Reproducible data pipeline

Given the size and complexity of the datasets, data processing, and data analysis methods, we integrated all analyses and raw data into a Data Version Control pipeline[69]. The pipeline uses both Nextflow and Docker images to guarantee a reproducible execution environment. This enabled us to keep all results consistent because any change or exploration of a data-processing method automatically triggered the recalculation of all dependent analyses and integrations.

Mice primary cortical cultures

Primary cortical neuronal cell cultures were generated from neonatal mouse C57BL/6J pups aged postnatal day 0–1 (P0–P1) in accordance with ethical guidelines for animal experimentation at local and international levels. Animal care strictly followed official governmental protocols, with utmost effort to minimize the number of animals utilized and to mitigate any potential suffering or distress. Pups were decapitated, and the brains were collected in dissection media containing 10× Hanks balanced salt solution and $NaHCO_3$. The cortex was dissected, the meninges were removed, and small pieces of the cortex were collected in a Falcon tube. Tissues were trypsinized at 37 °C in a water bath for 12 min and treated with 200 µL DNAse I (10 mg/mL). The tissue strips were gently triturated (until the tissue fragmented) in fetal bovine serum using a fire-polished Pasteur pipette. The mixture was subsequently centrifuged at 800 × *g* for four minutes, and the resulting cell pellet was resuspended and cultured in a neurobasal medium supplemented with B27 and antibiotics (0.06 µg/mL penicillin and 0.1 µg/mL streptomycin). Cells were seeded at a density of 3×10^5 cells per well in 24-well plates. Prior to cell seeding, the coverslips were acid-washed, rinsed several times with water, sterilized with ethanol and UV light, and placed in a well plate. The plates were then coated with poly-L-ornithine (0.05 mg/mL) overnight and laminin (10 µg/mL) for 2 h in an incubator before use. The cells were maintained at 37 °C in a humidified incubator under 5% CO_2 for seven days prior to the experiments. The cell culture medium was replaced every three days during this period. To induce glutamate excitotoxicity, L-glutamic acid (Tocris, UK) was dissolved in 50 mM NaOH, and a stock solution of 50 mM was prepared prior to use. An appropriate concentration of glutamate was prepared in the maintenance medium (neurobasal medium supplemented with B27 and antibiotics). The cells were exposed to 5 mM glutamate by exchanging 1:3 medium at seven days in vitro. After six hours of incubation, glutamate was thoroughly removed by washing, and the cells were fixed for immunocytochemistry or lysed for protein extraction.

Immunocytochemistry and microscopy for in vitro experiments

Cells were cultured on coverslips following previously described methods[70] and immunostained at seven days in vitro according to standard techniques. Cells were fixed in 4% paraformaldehyde in PBS at room temperature for 10 min. To quench the free aldehyde groups, the cells were treated with 50 mM NH_4Cl for 15 min and washed with PBS. For the permeabilization of the cell membrane, PBS with 0.25% Triton X-100 was added for 10 min at room temperature. Non-specific binding sites were blocked by applying 10% goat serum in PBS for at least 20 min. Dilutions of primary antibodies were prepared in blocking solution to a final volume of 180 µL per 18-mm coverslip, and cells were incubated for 90 min at 37 °C with shaking. The following primary antibodies were used: mouse anti-MAP2 (Invitrogen, Waltham, MA, USA; #MA5-12826) (1:500) and rabbit anti-cleaved caspase 3 (Cell Signaling Technology, Danvers, MA, USA; #9661) (1:250). The cells were washed three times for five minutes each with PBS before applying the secondary antibodies. The cells were then incubated with secondary antibodies for 30 min and washed. For double staining, a second primary antibody was added, and the same steps were repeated. Coverslips were mounted on slides using a mounting medium supplemented with DAPI. Images were captured using an inverted fluorescence microscope (Zeiss, Jena, Germany) with a 63× oil objective and analyzed using ImageJ software. Fifteen random images from each coverslip were analyzed for cell death by counting the number of cleaved caspase-3 positive cells. Neurite lengths were measured using a simple neurite tracing plugin in ImageJ. Statistical analyses were conducted using GraphPad Prism version 9.4.1 (GraphPad, San Diego, CA, USA). Outliers were identified and removed using the Grubbs test ($\alpha = 0.1$). Comparisons were done using one-way analysis of variance (ANOVA), and data were plotted as the mean ± standard error of the mean (SEM) of at least five independent experiments. Differences were considered statistically significant at $p < 0.05$.

Protein extraction and western blotting

For protein analysis, cells were washed once with 1× PBS, and after adding RIPA lysis buffer, protease inhibitor cocktail (1:25), and phosphatase inhibitor (1:20), cells were incubated on ice for five minutes. The cells were scraped off with a cell scraper, transferred into 1-mL reaction tubes, and homogenized by passage through a U-100 insulin syringe several times. Protein concentration was determined using a Pierce BCA Protein Assay Kit (Thermo Fisher Scientific) following the manufacturer's instructions. One microliter of protein sample was used for the assay. Colorimetric reactions were analyzed using an Infinite M200 PRO ELISA plate reader (Tecan, Männedorf, Switzerland). Twenty grams of each sample were loaded onto a gel (NuPAGE 4 to 12%, Bis-Tris, Invitrogen). NuPAGE LDS sample buffer (1:4) and sample-reducing buffer (1:10) were added to lysed protein before loading onto the gels, incubated with shaking at 75 °C for 13 min, and centrifuged at 12 000 × *g* at 4 °C. The proteins were subjected to gel electrophoresis at 200 V. Subsequently, the proteins were transferred onto nitrocellulose membranes using an iBlot2 gel transfer device (Thermo Fisher Scientific). The membranes were then blocked with 5% nonfat milk in PBST at room temperature for 30 min. For antibody incubation, primary antibodies (diluted in blocking buffer) were added to the membranes and allowed to incubate overnight at 4 °C with rotation. After four washes with PBST (five minutes each), the membranes were incubated with highly sensitive horseradish peroxidase-labeled secondary antibodies (diluted 1:10 000 in blocking buffer) at room temperature for one hour. Finally, the membranes were washed thoroughly with PBST to remove the unbound antibodies. Blots were incubated with enhanced chemiluminescence reagent and were imaged using a Molecular Imager ChemiDoc (Bio-Rad) imaging system. Band signal intensities were quantified using ImageJ software and normalized to housekeeping proteins and controls. Statistical analyses were conducted using GraphPad Prism version 9.4.1. Outliers were identified and removed using the Grubbs test ($\alpha = 0.1$). Comparisons were done

using one-way ANOVA, and data were plotted as the mean ± SEM of at least three independent experiments. Differences were considered statistically significant at $p < 0.05$.

Tissue protein extraction for immunoblot analysis

Spinal cords were homogenized in five volumes (w/v) of 1% boiling SDS[71]. Protein homogenates were sonicated, boiled for 10 min, and centrifuged at 13 500 × *g* for five minutes. Supernatants were analyzed by dot blotting. For detergent-insoluble protein extraction, mouse tissues were homogenized in 10 volumes (w/v) of buffer (15 mM Tris–HCl pH 7.6, 1 mM dithiothreitol, 0.25 M sucrose, 1 mM $MgCl_2$, 2.5 mM EDTA, 1 mM EGTA, 0.25 M Na_3VO_4, 2 mM $Na_4P_2O_7$, 25 mM NaF, 5 μM MG132) and a protease inhibitor cocktail (Roche, Basel, Switzerland), as previously described[72]. Briefly, the samples were centrifuged at 10 000 × *g*, and the pellet was suspended in an ice-cold homogenization buffer containing 2% Triton X-100 and 150 mM KCl. The samples were then centrifuged at 10 000 × *g* to obtain the Triton-insoluble (insoluble) fraction.

Immunohistochemistry

Mice were anesthetized and underwent transcardial perfusion using 50 mL PBS followed by 100 mL of 4% paraformaldehyde (in PBS). The spinal cord was promptly dissected, postfixed for three hours, and subsequently transferred to a solution of 20% sucrose in PBS overnight. Once sank, the spinal cord was transferred to a 30% sucrose solution until it reached the desired consistency. Next, the spinal cord was frozen in n-pentane at 45 °C and stored at ∼-80 °C. Prior to freezing, the spinal cord was divided into cervical, thoracic, and lumbar segments and embedded in Tissue-Tek O.C.T. compound (Sakura Finetek, Torrance, CA, USA). Coronal sections (30-μm thick) were sliced from the lumbar spinal cord and subjected to immunohistochemistry. Rabbit monoclonal anti-pMEK (Ser221) (pMEK2) antibody (1:50, Cell Signaling; RRID: AB_490903) was used. In brief, slices were incubated with blocking solutions (0.2% Triton X-100 and 2% normal goat serum) at room temperature for one hour. Subsequently, the slices were incubated overnight at 4 °C with primary antibodies. The sections were then incubated with biotinylated secondary antibodies (1:200) for one hour at room temperature, followed by immunostaining using an avidin–biotin kit and diaminobenzidine. To facilitate visualization, sections were counterstained with 0.5% cresyl violet. Stained sections were captured at 20× and 40× magnification using an Olympus BX-61 Virtual Stage microscope (Olympus Life Sciences, Tokyo, Japan), ensuring complete stitching of the entire section with a pixel size of 0.346 μm. Images were acquired using 6-μm-thick stacks (step size of 2 μm). The different focal planes were merged into a single stack using mean intensity projection to maintain consistent focus across the sample. Finally, the acquired signals were analyzed for each slice using ImageJ and OlyVIA software (Olympus Life Sciences).

Immunoblotting for in vivo experiments

Protein levels were quantified using a BCA Protein Assay Kit (Pierce Biotechnology, Waltham, MA, USA) and analyzed by western blotting and dot blotting following previously described methods[73]. Membranes were blocked with a solution of 3% (w/v) BSA (Sigma-Aldrich) and 0.1% (v/v) Tween 20 in Tris-buffered saline (pH 7.5). Subsequently, the membranes were incubated with primary antibodies followed by peroxidase-conjugated secondary antibodies (GE HealthCare, Chicago, IL, USA). The antibodies utilized were rabbit monoclonal anti-pMEK2 (1:2000, Cell Signaling Technology; RRID: AB_490903), rabbit monoclonal anti-phospho-p44/42 MAPK (Erk1/2) (Thr202/Tyr204) (1:2000, Cell Signaling Technology; RRID: AB_2315112), rabbit polyclonal anti-human SOD1 (1:1000, StressMarq Biosciences, Victoria, Canada; RRID: AB_2704217), rabbit polyclonal anti-ubiquitin (1:1000, Abcam, Cambridge,

UK; RRID: AB_306069), and mouse monoclonal anti-SQSTM1/p62 (p62) (1:500, Abcam). Peroxidase-conjugated secondary antibodies (goat anti-mouse and anti-rabbit) (GE HealthCare) were used at dilutions of 1:20 000 and 1:10 000, respectively. The blots were developed using the Luminata Forte Western Chemiluminescent HRP Substrate (MilliporeSigma, Burlington, MA, USA) and visualized on a ChemiDoc Imaging System (Bio-Rad). Densitometry analysis was performed using Image Lab software version 6.0 (Bio-Rad). Protein immunoreactivity was normalized to Ponceau Red staining (Honeywell Fluka, Charlotte, NC, USA) for accurate quantification.

Preclinical study in SOD1^{G93A} mice

Starting at the presymptomatic stage (nine weeks of age), SOD1^{G93A} female and male mice received a 3 mg/kg dose of trametinib (n = 10) or vehicle (PBS) (n = 10) via intranasal delivery. The drug was administered twice per week for seven weeks (from 9 to 16 weeks of age). At 16 weeks of age, the mice were sacrificed, and spinal cords and plasma were collected for subsequent biochemical analysis. The animal experimental protocols used in this study (Prot. no. 9F5F5.143 and 9F5F5.250) were prospectively reviewed and approved by the Mario Negri Institutional Animal Care and Use Committee and the Italian Ministry of Health (*Direzione Generale della Sanità Animale e dei Farmaci Veterinari, Ufficio 6).* This study complied with international and local animal welfare standards.

Plasma neurofilament light chain quantification

Mouse plasma samples were collected in K2-EDTA BD Microtainer blood collection tubes and centrifuged at 5 000 × *g* for five minutes to obtain the plasma. The plasma NfL was quantified using a Simoa NF-light Advantage (SR-X) Kit (#103400) on a Quanterix SR-X platform (Quanterix, Boston, MA, USA). All reagents used were from a single lot, and measurements were performed according to the manufacturer's protocol.

Statistical analyses of in vivo experiments

Statistical analyses of in vivo experimental data were performed using GraphPad Prism 7.0. Student's *t*-tests or one-way ANOVAs, followed by posthoc tests, were used to analyze the differences between the experimental groups for each variable. Statistical significance was set at $p < 0.05$.

Data availability

Raw RNA-Seq and processed gene expression data were deposited to the National Center for Biotechnology Information Gene Expression Omnibus database (GSE234246). Encrypted raw RNA-Seq data for the human cohort were deposited to the European Genome Phenome Archive (registered study: EGAS00001007318). Proteomics and phosphoproteomics datasets have been deposited in the ProteomeXchange Consortium database with the identifiers PXD043300 and PXD043297, respectively.

Code availability

For RNA-Seq, we used the Nextflow pipeline for alignment and DESeq2 for differential analysis: https://www.nextflow.io/, https://www.bioconductor.org/packages//2.10/bioc/html/DESeq.html
Alternative splicing was performed using SUPPA, DRIMSeq, and DEXSeq (https://github.com/comprna/SUPPA, https://bioconductor.org/packages/release/bioc/html/DRIMSeq.html, https://bioconductor.org/packages/release/bioc/html/DEXSeq.html

Enrichment was performed with:
https://bioconductor.org/packages/release/bioc/html/clusterProfiler.html, http://revigo.irb.hr/
Gene–gene interaction network analysis was done with:
https://cran.r-project.org/web/packages/WGCNA/index.html
Deconvolution was performed with Scaden:
https://scaden.readthedocs.io/en/latest/

References

1. Mehta, P. *et al.* Prevalence of amyotrophic lateral sclerosis in the United States using established and novel methodologies, 2017. *Amyotroph. Lateral Scler. Front. Degener.* **24**, 108–116 (2023).
2. Suzuki, N., Nishiyama, A., Warita, H. & Aoki, M. Genetics of amyotrophic lateral sclerosis: seeking therapeutic targets in the era of gene therapy. *J. Hum. Genet.* **68**, 131–152 (2023).
3. Mead, R. J., Shan, N., Reiser, H. J., Marshall, F. & Shaw, P. J. Amyotrophic lateral sclerosis: a neurodegenerative disorder poised for successful therapeutic translation. *Nat. Rev. Drug Discov.* **22**, 185–212 (2023).
4. Braak, H. & Braak, E. Neuropathological stageing of Alzheimer-related changes. *Acta Neuropathol. (Berl.)* **82**, 239–259 (1991).
5. Braak, H. *et al.* Staging of brain pathology related to sporadic Parkinson's disease. *Neurobiol. Aging* **24**, 197–211 (2003).
6. Brettschneider, J. *et al.* Stages of pTDP-43 pathology in amyotrophic lateral sclerosis. *Ann. Neurol.* **74**, 20–38 (2013).
7. Aronica, E. *et al.* Molecular classification of amyotrophic lateral sclerosis by unsupervised clustering of gene expression in motor cortex. *Neurobiol. Dis.* **74**, 359–376 (2015).
8. Morello, G. *et al.* Integrative multi-omic analysis identifies new drivers and pathways in molecularly distinct subtypes of ALS. *Sci. Rep.* **9**, 9968 (2019).
9. Tam, O. H. *et al.* Postmortem Cortex Samples Identify Distinct Molecular Subtypes of ALS: Retrotransposon Activation, Oxidative Stress, and Activated Glia. *Cell Rep.* **29**, 1164-1177.e5 (2019).
10. Prudencio, M. *et al.* Distinct brain transcriptome profiles in C9orf72-associated and sporadic ALS. *Nat. Neurosci.* **18**, 1175–1182 (2015).
11. Figueroa-Romero, C. *et al.* Expression of microRNAs in human post-mortem amyotrophic lateral sclerosis spinal cords provides insight into disease mechanisms. *Mol. Cell. Neurosci.* **71**, 34–45 (2016).
12. Umoh, M. E. *et al.* A proteomic network approach across the ALS-FTD disease spectrum resolves clinical phenotypes and genetic vulnerability in human brain. *EMBO Mol. Med.* **10**, 48–62 (2018).
13. Eshima, J. *et al.* Molecular subtypes of ALS are associated with differences in patient prognosis. *Nat. Commun.* **14**, 95 (2023).
14. Kenna, K. P. *et al.* NEK1 variants confer susceptibility to amyotrophic lateral sclerosis. *Nat. Genet.* **48**, 1037–1042 (2016).
15. Langfelder, P. & Horvath, S. WGCNA: an R package for weighted correlation network analysis. *BMC Bioinformatics* **9**, 559 (2008).
16. Buratti, E. & Baralle, F. E. The multiple roles of TDP-43 in pre-mRNA processing and gene expression regulation. *RNA Biol.* **7**, 420–429 (2010).
17. Polymenidou, M. *et al.* Misregulated RNA processing in amyotrophic lateral sclerosis. *Brain Res.* **1462**, 3–15 (2012).
18. Ma, X. R. *et al.* TDP-43 represses cryptic exon inclusion in the FTD-ALS gene UNC13A. *Nature* **603**, 124–130 (2022).
19. Menden, K. *et al.* Deep learning-based cell composition analysis from tissue expression profiles. *Sci. Adv.* **6**, eaba2619 (2020).
20. Månberg, A. *et al.* Altered perivascular fibroblast activity precedes ALS disease onset. *Nat. Med.* **27**, 640–646 (2021).
21. Rinchetti, P., Rizzuti, M., Faravelli, I. & Corti, S. MicroRNA Metabolism and Dysregulation in Amyotrophic Lateral Sclerosis. *Mol. Neurobiol.* **55**, 2617–2630 (2018).

22. Hirano, M. *et al.* Mutations in the gene encoding p62 in Japanese patients with amyotrophic lateral sclerosis. *Neurology* **80**, 458–463 (2013).
23. Beckers, J., Tharkeshwar, A. K. & Van Damme, P. C9orf72 ALS-FTD: recent evidence for dysregulation of the autophagy-lysosome pathway at multiple levels. *Autophagy* **17**, 3306–3322 (2021).
24. Reijnders, M. J. M. F. & Waterhouse, R. M. Summary Visualizations of Gene Ontology Terms With GO-Figure! *Front. Bioinforma.* **1**, 638255 (2021).
25. Biogen. *A Phase 1, Double-Blind, Placebo-Controlled, Single-Ascending-Dose Study to Evaluate the Safety, Tolerability, Pharmacokinetics, and Pharmacodynamics of BIIB100 Administered Orally to Adult Participants With Amyotrophic Lateral Sclerosis*. https://clinicaltrials.gov/ct2/show/NCT03945279 (2023).
26. Argelaguet, R. *et al.* Multi-Omics Factor Analysis-a framework for unsupervised integration of multi-omics data sets. *Mol. Syst. Biol.* **14**, e8124 (2018).
27. Shu, R. *et al.* APP intracellular domain acts as a transcriptional regulator of miR-663 suppressing neuronal differentiation. *Cell Death Dis.* **6**, e1651 (2015).
28. Kenigsbuch, M. *et al.* A shared disease-associated oligodendrocyte signature among multiple CNS pathologies. *Nat. Neurosci.* **25**, 876–886 (2022).
29. Costa, J. *et al.* Cerebrospinal Fluid Chitinases as Biomarkers for Amyotrophic Lateral Sclerosis. *Diagn. Basel Switz.* **11**, 1210 (2021).
30. Yoshida, T. *et al.* Identification and characterization of a novel chemotype MEK inhibitor able to alter the phosphorylation state of MEK1/2. *Oncotarget* **3**, 1533–1545 (2012).
31. Dong, X., Wang, Y. & Qin, Z. Molecular mechanisms of excitotoxicity and their relevance to pathogenesis of neurodegenerative diseases. *Acta Pharmacol. Sin.* **30**, 379–387 (2009).
32. Gurney, M. E. *et al.* Motor neuron degeneration in mice that express a human Cu,Zn superoxide dismutase mutation. *Science* **264**, 1772–1775 (1994).
33. Chun, Y. S. *et al.* MEK1/2 inhibition rescues neurodegeneration by TFEB-mediated activation of autophagic lysosomal function in a model of Alzheimer's Disease. *Mol. Psychiatry* **27**, 4770–4780 (2022).
34. Gal, J., Ström, A.-L., Kilty, R., Zhang, F. & Zhu, H. p62 accumulates and enhances aggregate formation in model systems of familial amyotrophic lateral sclerosis. *J. Biol. Chem.* **282**, 11068–11077 (2007).
35. Benatar, M., Wuu, J. & Turner, M. R. Neurofilament light chain in drug development for amyotrophic lateral sclerosis: a critical appraisal. *Brain J. Neurol.* awac394 (2022) doi:10.1093/brain/awac394.
36. Santiago, J. A., Quinn, J. P. & Potashkin, J. A. Network Analysis Identifies Sex-Specific Gene Expression Changes in Blood of Amyotrophic Lateral Sclerosis Patients. *Int. J. Mol. Sci.* **22**, 7150 (2021).
37. Murdock, B. J., Goutman, S. A., Boss, J., Kim, S. & Feldman, E. L. Amyotrophic Lateral Sclerosis Survival Associates With Neutrophils in a Sex-specific Manner. *Neurol. Neuroimmunol. Neuroinflammation* **8**, e953 (2021).
38. Günther, R. *et al.* The rho kinase inhibitor Y-27632 improves motor performance in male SOD1(G93A) mice. *Front. Neurosci.* **8**, 304 (2014).
39. Torres, P. *et al.* Gender-Specific Beneficial Effects of Docosahexaenoic Acid Dietary Supplementation in G93A-SOD1 Amyotrophic Lateral Sclerosis Mice. *Neurother. J. Am. Soc. Exp. Neurother.* **17**, 269–281 (2020).
40. Food and Drug Administration; U.S. Department of Health and Human Services. Amyotrophic Lateral Sclerosis: Developing Drugs for Treatment Guidance for Industry. (2019).

41. Tahedl, M. *et al.* Propagation patterns in motor neuron diseases: Individual and phenotype-associated disease-burden trajectories across the UMN-LMN spectrum of MNDs. *Neurobiol. Aging* **109**, 78–87 (2022).
42. Sahana, T. G. & Zhang, K. Mitogen-Activated Protein Kinase Pathway in Amyotrophic Lateral Sclerosis. *Biomedicines* **9**, 969 (2021).
43. Ayala, V. *et al.* Cell stress induces TDP-43 pathological changes associated with ERK1/2 dysfunction: implications in ALS. *Acta Neuropathol. (Berl.)* **122**, 259–270 (2011).
44. Pérez-Cabello, J. A. *et al.* MAPK/MAK/MRK overlapping kinase (MOK) controls microglial inflammatory/type-I IFN responses via Brd4 and is involved in ALS. *Proc. Natl. Acad. Sci.* **120**, e2302143120 (2023).
45. Bonifacino, T. *et al.* Nearly 30 Years of Animal Models to Study Amyotrophic Lateral Sclerosis: A Historical Overview and Future Perspectives. *Int. J. Mol. Sci.* **22**, 12236 (2021).
46. Gordon, D. *et al.* Single-copy expression of an amyotrophic lateral sclerosis-linked TDP-43 mutation (M337V) in BAC transgenic mice leads to altered stress granule dynamics and progressive motor dysfunction. *Neurobiol. Dis.* **121**, 148–162 (2019).
47. LaClair, K. D. *et al.* Congenic expression of poly-GA but not poly-PR in mice triggers selective neuron loss and interferon responses found in C9orf72 ALS. *Acta Neuropathol. (Berl.)* **140**, 121–142 (2020).
48. Mitchell, J. C. *et al.* Overexpression of human wild-type FUS causes progressive motor neuron degeneration in an age- and dose-dependent fashion. *Acta Neuropathol. (Berl.)* **125**, 273–288 (2013).
49. Ewels, P. A. *et al.* The nf-core framework for community-curated bioinformatics pipelines. *Nat. Biotechnol.* **38**, 276–278 (2020).
50. Andrews, S. FastQC: A Quality Control Tool for High Throughput Sequence Data. (2010).
51. Patro, R., Duggal, G., Love, M. I., Irizarry, R. A. & Kingsford, C. Salmon provides fast and bias-aware quantification of transcript expression. *Nat. Methods* **14**, 417–419 (2017).
52. Wu, T. *et al.* clusterProfiler 4.0: A universal enrichment tool for interpreting omics data. *Innov. Camb. Mass* **2**, 100141 (2021).
53. Cox, J. & Mann, M. MaxQuant enables high peptide identification rates, individualized p.p.b.-range mass accuracies and proteome-wide protein quantification. *Nat. Biotechnol.* **26**, 1367–1372 (2008).
54. Cox, J. *et al.* Andromeda: A Peptide Search Engine Integrated into the MaxQuant Environment. *J. Proteome Res.* **10**, 1794–1805 (2011).
55. Stekhoven, D. J. & Bühlmann, P. MissForest--non-parametric missing value imputation for mixed-type data. *Bioinforma. Oxf. Engl.* **28**, 112–118 (2012).
56. Ritchie, M. E. *et al.* limma powers differential expression analyses for RNA-sequencing and microarray studies. *Nucleic Acids Res.* **43**, e47–e47 (2015).
57. Tyanova, S. *et al.* The Perseus computational platform for comprehensive analysis of (prote)omics data. *Nat. Methods* **13**, 731–740 (2016).
58. Griffiths-Jones, S., Grocock, R. J., van Dongen, S., Bateman, A. & Enright, A. J. miRBase: microRNA sequences, targets and gene nomenclature. *Nucleic Acids Res.* **34**, D140-144 (2006).
59. Langmead, B., Trapnell, C., Pop, M. & Salzberg, S. L. Ultrafast and memory-efficient alignment of short DNA sequences to the human genome. *Genome Biol.* **10**, R25 (2009).
60. Love, M. I., Huber, W. & Anders, S. Moderated estimation of fold change and dispersion for RNA-seq data with DESeq2. *Genome Biol.* **15**, 550 (2014).
61. Chen, Y. & Wang, X. miRDB: an online database for prediction of functional microRNA targets. *Nucleic Acids Res.* **48**, D127–D131 (2020).

62. Huang, H.-Y. *et al.* miRTarBase update 2022: an informative resource for experimentally validated miRNA–target interactions. *Nucleic Acids Res.* **50**, D222–D230 (2022).
63. Liu, W. & Wang, X. Prediction of functional microRNA targets by integrative modeling of microRNA binding and target expression data. *Genome Biol.* **20**, 18 (2019).
64. Bhattacherjee, A. *et al.* Cell type-specific transcriptional programs in mouse prefrontal cortex during adolescence and addiction. *Nat. Commun.* **10**, 4169 (2019).
65. Mathys, H. *et al.* Single-cell transcriptomic analysis of Alzheimer's disease. *Nature* **570**, 332–337 (2019).
66. Wolf, F. A., Angerer, P. & Theis, F. J. SCANPY: large-scale single-cell gene expression data analysis. *Genome Biol.* **19**, 15 (2018).
67. Szklarczyk, D. *et al.* STRING v11: protein-protein association networks with increased coverage, supporting functional discovery in genome-wide experimental datasets. *Nucleic Acids Res.* **47**, D607–D613 (2019).
68. Szklarczyk, D. *et al.* The STRING database in 2021: customizable protein–protein networks, and functional characterization of user-uploaded gene/measurement sets. *Nucleic Acids Res.* **49**, D605–D612 (2021).
69. Kuprieiev, R. *et al.* DVC: Data Version Control - Git for Data & Models. (2022) doi:10.5281/zenodo.7083235.
70. Zhang, J.-N. *et al.* Calpain-mediated cleavage of collapsin response mediator protein-2 drives acute axonal degeneration. *Sci. Rep.* **6**, 37050 (2016).
71. Filareti, M. *et al.* Decreased Levels of Foldase and Chaperone Proteins Are Associated with an Early-Onset Amyotrophic Lateral Sclerosis. *Front. Mol. Neurosci.* **10**, 99 (2017).
72. Pasetto, L. *et al.* Defective cyclophilin A induces TDP-43 proteinopathy: implications for amyotrophic lateral sclerosis and frontotemporal dementia. *Brain J. Neurol.* **144**, 3710–3726 (2021).
73. Luotti, S. *et al.* Diagnostic and prognostic values of PBMC proteins in amyotrophic lateral sclerosis. *Neurobiol. Dis.* **139**, 104815 (2020).

Acknowledgements

We thank all the members of the Lingor, Bonn, Carapito, Schlapbach, Pasterkamp, and Bonnetto laboratories for their feedback on the manuscript. This work was performed by the research consortium "Multi-omic analysis of axono-synaptic degeneration in motoneuron disease (MAXOMOD)" funded in the scope of the E-Rare Joint Transnational Call for Proposals 2018 "Transnational research projects on hypothesis-driven use of multi-omic integrated approaches for discovery of disease causes and/or functional validation in the context of rare diseases." Consortium members: S. B., J. P., V. B., C. C., R. S., and M. K., coordinated by P. L.

L. C. G., M. P., and P. L. were supported by the Bundesministerium für Bildung und Forschung (01GM1917A). P. L. and D. E. were further supported by the Munich Cluster for Systems Neurology (SyNergy). S. H. was supported by SFB1192 B8; S. O. by SFB1286 SP02 and KFO296 P8; R. K. by FOR5068 P9; F. H. by the M3I excellence initiative and a UKE postdoctoral stipend; C. H. by KFO306 P11; and S. B. by SFB1286 SP02, SFB1192 PB8, and PC3. J. P. was supported by Stichting ALS Nederland (TOTALS). D. E. received funding from the European Union's Horizon Europe research and innovation program under grant agreement No 101057649 and the Association for Frontotemporal Degeneration (AFTD).

The funders had no role in the study design, data collection and analysis, decision to publish, or manuscript preparation.

Author contributions

P. L. and L. C. G. conceived the project, and S. H., S. O., and S. B. conceptualized the computational analysis. P. L., L. C. G., J. K., and A. D. designed the sample collection methodology, reviewed the sample and data quality, and coordinated the acquisition of human tissue samples from the brain banks as well as pathological, genetic, and clinical information.
L. C. G, M. P., and Q. Z. processed mouse and human brain samples for multiomics experiments with the infrastructure provided by V. B., C. C., D. E., and P. L.
C. D., M. S., T. B. H., I. C., and M. D. analyzed the genetic data.
S. H., S. O., R. K., and F. H. were responsible for the computational data analysis, and conceived and planned the statistical analyses. L. C. G, S. H., F. H., R. K., P. L., M. P., and L. P. contributed to figure generation and assembly.
M. P, L. P., L. C. G., S. S., and S. C. conducted the validation experiments with conceptual inputs from P. L. and V. B.
L. C. G., S. H., S. B., and P. L. wrote the manuscript with input from all co-authors.

Competing interests

The authors declare no competing interests.

Additional information

Supplementary information

Correspondence and requests for materials should be addressed to Paul Lingor.

Figure Legends

Fig. 1 Study overview and the transcriptomic landscape of brains affected by amyotrophic lateral sclerosis

a. Overview of the sample processing workflow. Prefrontal cortex samples were prepared for multiomics experiments from the human cohort (51 ALS/50 CTR samples), as well as from four selected ALS mouse models (C9orf72, FUS, SOD1, and TDP-43; 10 TG/10 CTR animals per group). RNA, DNA, and protein lysates were prepared for mRNA and small RNA sequencing, targeted DNA sequencing, and proteomics/phosphoproteomic (ph-proteomic) experiments. The latter was performed exclusively on animal tissues.
b. Volcano plot of deregulated genes in human samples. x-axis: log2(fold change); y-axis: -log10(adjusted *p*-values) for each gene. Blue and orange circles indicate significant differential expression: left side, decrease (low ALS); right side, increase (high ALS).
c. Heat map of the activity scores (calculated by Decoupler) of each pathway throughout the ALS human cohort. Pathways were selected based on their increased occurrence across different enrichment analyses. Pathways are indicated on the y-axis and ALS samples on the x-axis (top) along with metadata, sex, and age at death. Only selected pathways are shown. A full heat map of all chosen pathways is shown in Supplementary Figure 16.
d. Dot plot analysis of enriched Kyoto Encyclopedia of Genes and Genomes (KEGG) pathways using ClusterProfiler in male and female samples. The dot plot displays significantly enriched pathways in males and females, represented by circles colored by their corresponding adjusted *p*-values (-log10 transformed) on the x-axis and gene count on the y-axis. The size of each circle corresponds to the number of genes annotated in the KEGG gene set. Similar pathways were also identified. Pathway clusters for human males were composed of the following terms: retrograde endocannabinoid signaling, synaptic vesicle cycle, long-term potentiation, glutamatergic synapse (*synapse related terms*), *Staphylococcus aureus*

infection, malaria, complement and coagulation cascades, and cytokine–cytokine receptor interaction (for *immune system activation/infectious diseases*). Pathway clusters for human females were composed of the following terms: Parkinson's disease, Huntington's disease, spinocerebellar ataxia, pathway of neurodegeneration-multiple diseases, and amyotrophic lateral sclerosis (for *neurodegenerative/neurological diseases*); complement and coagulation cascades, viral protein interaction with cytokine and cytokine receptor, *Staphylococcus aureus* infection, Epstein–Barr virus infection, Influenza A cytokine–cytokine receptor interaction (for *immune system activation/infectious diseases*). **e.** Heat map showing Pearson's correlation between the weighted gene co-expression network analysis (WGCNA) modules and each sample group. Each cluster of the ALS samples and controls is shown on the y-axis (substratified by sex). Representative WGCNA modules were selected for the identified ALS clusters (turquoise (1) and yellow (2) for clusters C1 and C2, and tan (3) and light cyan (4) for clusters C3 and C4) and explored further by enrichment analyses.
f. Enrichment results (over-representation analysis) for each selected WGCNA module (top five terms based on significance).

Fig. 2 Overview of the results for the selected ALS mouse models, correlation with human results, and evidence for mitogen-activated protein kinase deregulation in ALS subclusters

a. Volcano plot of deregulated genes in the four transgenic mouse models, represented by dots colored according to sex. The x-axis shows the log2(fold change) between transgenic and wild-type mice, whereas the y-axis shows the -log10(adjusted *p*-values). Orange and blue dots represent DEGs in females and males, respectively.
b. Dot plot analysis of enriched gene ontology (GO) biological processes (BP) using Genetonics in male and female samples for ALS mouse models. The dot plot displays enriched pathways in males and females, represented by circles colored by their corresponding adjusted *p*-values on the x-axis and gene count on the y-axis. The size of each circle corresponds to the number of genes annotated in the GO BP gene sets.
c. Heat map showing changes in cell type proportions across ALS mouse models and human clusters. The indicated changes are the relative differences between the median cell type composition of the ALS cluster/TG and the median cell type composition in the corresponding CTR samples. Comparisons were grouped according to their similarity using hierarchical clustering with Euclidean distance.
d. Heat map showing the pairwise Pearson correlation of relative changes in median cell type proportions in ALS mouse models and human clusters. Comparisons were grouped according to similarity using hierarchical clustering, as depicted by the dendrograms.
e. Summarized visualization of the MAPK pathway (Kyoto Encyclopedia of Genes and Genomes: hsa04010) colored by log2(fold change) of transcriptomics clusters C1 (orange) and C3 (purple) compared with healthy controls.

Fig. 3 Differential alternative splicing and miRNAomic profiling

a,b. Differential alternative splicing (DAS) analysis. The plot displays the results for human male and female samples for various splice events, i.e., alternative exon (AE), skipped exon (SE), alternative 5'-splice site (A5), alternative 3'-splice site (A3), alternative last exon (AL), and retained intron (RI) events. Each event is represented by a separate bar, the height of which represents the fraction of significant events in ALS vs. CTR. Blue bars represent events with significant differential splicing in males, whereas orange bars represent events with significant differential splicing in females.
c. Venn diagram showing the overlap of DAS genes in four transgenic mouse models (TDP-43, FUS, C9orf72, and SOD1) for the ALS vs. CTR comparison. Each circle represents the

number of genes with significantly differential splicing in each model. Overlapping regions between circles represent the number of genes with significantly differential splicing in more than one model.

d. Enrichment of selected themes for DAS genes in four transgenic mouse models and humans, male and female samples, and percentage of genes in each functional term. The plot displays two sets of information: the enrichment of DAS genes in different samples and the percentage of genes in each functional term. The y-axis represents the percentage of genes in each term, whereas the x-axis represents different functional terms. The bars are colored according to sex, mouse models, and human samples.

e,f. Volcano plots showing differential expression of mature miRNAs (e) and hairpin miRNAs (f) in male and female human samples. The plots display the log2(fold change) (x-axis) and the -log10(adjusted *p*-value) (y-axis) for each miRNA between male and female samples. The miRNAs are represented as dots in the plot, and the color of the dots indicates the significance of differential expression (blue for males and orange for females).

g,h. The heat maps display the log2(fold change) of the top miRNAs in female and male samples from the mouse and human datasets. The miRNAs were selected based on the ordered absolute log2(fold change) per dataset. Red indicates miRNA upregulation, whereas blue indicates miRNA downregulation. Statistical significance of the differential expression of miRNAs was inferred using DESeq2 and is indicated by asterisks. $^{**}p < 0.01$ and $^{*}p < 0.05$ represents statistical significance at a high and moderate level, respectively. The top five miRNAs significantly differentially expressed in at least two mouse models are shown.

i. Protein–protein interaction network of the target genes of miRNA451a. MAPK1, AKT1, IKBKB, MYC, BCL2, and IL6 are important molecular hubs.

Fig. 4 Proteomics overview and multiomics factor integration

a. Volcano plot of deregulated proteins in human samples. x-axis: log2(fold change); y-axis: -log10(adjusted *p*-value) for each protein. Blue and orange circles indicate significant differential changes: left side, decrease (low ALS); right side, increase (high ALS).

b,c. Revigo-based summary of proteomic gene set enrichment results for human samples (left and right females). The plot summarizes the functional similarity of the proteins by reducing the redundant gene ontology (GO) biological processes (BP) terms and clustering the remaining non-redundant terms. The plot is divided into several areas, each of which represents a cluster of similar GO BP terms. The size of the circles represents the number of genes in the GO BP terms, and the color represents significance.

d,e. Plots displaying the results of GO enrichment analysis of the proteins identified in the proteomic data of the four mouse models (TDP-43, FUS, C9orf7, and SOD1) separated by sex. GO terms were summarized by clustering pathways in semantic space based on their descriptions using the GO-Figure clustering tool.

f. Pearson correlation of log2(fold change) of proteins found to be significantly deregulated ($p < 0.1$) in any mouse model or human sample. Comparisons were grouped according to similarity using hierarchical clustering, as depicted by the dendrograms.

g. Multi-Omics Factor Analysis (MOFA) was performed to integrate and visualize transcriptomic, proteomic, and mature and hairpin miRNA data in male and female samples. Uniform Manifold Approximation and Projection (UMAP) representation showing the distribution of male (blue) and female (orange) human samples.

h. Variance decomposition plot showing the contribution of each factor in the MOFA to the overall variance of the integrated dataset separated by sex. The plot displays the variance explained by transcriptomics, proteomics, and mature and hairpin miRNAs in human male and female samples. The y-axis represents the different omics, and the x-axis represents the

different factors in the analysis (left: male, right: female). Blue indicates the proportion of explained variance, and red indicates Pearson's correlation with the condition.

i. MOFA weight plot for human male miRNA data (factor 3) displayed the contribution of each gene to the MOFA model. Each line represents a gene, and the x-axis shows the MOFA weight of that gene, reflecting its importance to the factor.

j. MOFA weight plot for proteomic human female data (factor 12) displays the contribution of each protein to the MOFA model. Each line represents a protein, and the x-axis shows the MOFA weight of that protein, reflecting its importance to the factor.

k. Protein–protein interaction network of genes in factor 12 females. MAPK1 is an important molecular hub protein that interacts with PEA15, PRRT2, MEK2, DUSP6, HSPA4, and HSP90AA1. Proteins of interest are highlighted (bold and dark purple).

Fig. 5 Validation experiments

a,b. Effects of different concentrations of trametinib on apoptosis in glutamate (5 mM)- and non-glutamate-treated cells analyzed by immunostaining. Representative photomicrographs for two of the analyzed conditions (control [vehicle] and 200 nM trametinib). Scale bar: 40 µm.

c,d. Quantification plots showing the effects of treatment with trametinib on cell survival (caspase 3 staining) (**c**) and neurite outgrowth (**d**) for glutamate- or vehicle-treated (control) cells, for all analyzed conditions (control [vehicle]; 2 nM trametinib; 20 nM trametinib; 200 nM trametinib). Data are presented as the mean ± standard error of the mean (SEM) of at least five different cultures and were tested using one-way analysis of variance.

e,f. Western blot analysis and quantification of trametinib effects on pErk1/2 with and without glutamate treatment. Data represent the mean ± SEM of at least three different cultures and were tested by one-way analysis of variance, $p < 0.05$.

g,h. Diffuse pMEK2 immunostaining in the lumbar spinal cord of non-transgenic (**g**) and $SOD1^{G93A}$ mice (**h**) at 19 weeks of age. In the ventral horns, pMEK2 staining was mainly observed in motor neurons. Scale bar: 50 µm.

i. Western blot analysis of pMEK2 in the lumbar spinal cord of SOD^{1G93A} and non-transgenic mice at 9, 14, and 19 weeks of age. Data are mean ± SEM (n = 6–4 in each experimental group) and are expressed as relative immunoreactivity (RI). *$p < 0.05$, pairwise Tukey's test after one-way analysis of variance. Dot blot analysis of pERK1/2 (**j**), p62 (**k**), insoluble SOD1 (**l**), and ubiquitin (**m**) in the spinal cord of $SOD1^{G93A}$ female and male mice treated with trametinib or vehicle, at 16 weeks of age. Data represent mean ± SEM (n = 3/5 in each experimental group) and are expressed as relative immunoreactivity (RI). *$p < 0.05$, Student's *t*-test. Plasma neurofilament light chain levels were analyzed in female and male (**n**) $SOD1^{G93A}$ mice treated with or without trametinib at 16 weeks of age. Data are presented as the mean ± SEM (n = 3/5 in each experimental group). *$p < 0.05$, Student's *t*-test.

Table 1: Summary of the demographics of the human cohort

Continuous variables are presented as medians and ranges. Categorical variables were compared using Fisher's exact test (for single groups) or the chi-square test (for multiple groups); continuous variables were compared using the Mann–Whitney test. The *p*-values shown are uncorrected for multiple testing; *p*-values less than 0.05 are indicated in bold. Netherlands BB, Netherlands Brain Bank; Oxford BB, Oxford Brain Bank; PD and MS TB, Parkinson's and Multiple Sclerosis UK Tissue/Brain Banks; London ND BB, King's College London Brain Bank.

	Control	**ALS**	***p*-value**
Donors	50	51	
Age at death, years	75 (43–94)	67 (44–83)	**0.0032**
Sex female	56.0%	31.4%	**0.0163**
Postmortem interval, h	22 (5–95)	23 (2.5–98)	0.4324
Unknown	8.0%	5.9%	
Onset			
Bulbar	-	17.6%	
Spinal	-	37.3%	
Upper limb	-	31.6%	
Lower limb	-	63.1%	
Limb unknown	-	5.3%	
Thoracic	-	2.0%	
Unknown	-	43.1%	
Disease duration, years	-	3 (1–28)	
Unknown	-	39.2%	
Brain bank origin			**< 0.0001**
Netherlands BB	18.0%	17.6%	
Oxford BB	20.0%	27.5%	
ICL MS & PD TB	38.0%	0.0%	
London ND BB	24.0%	54.9%	

ALS, amyotrophic lateral sclerosis.

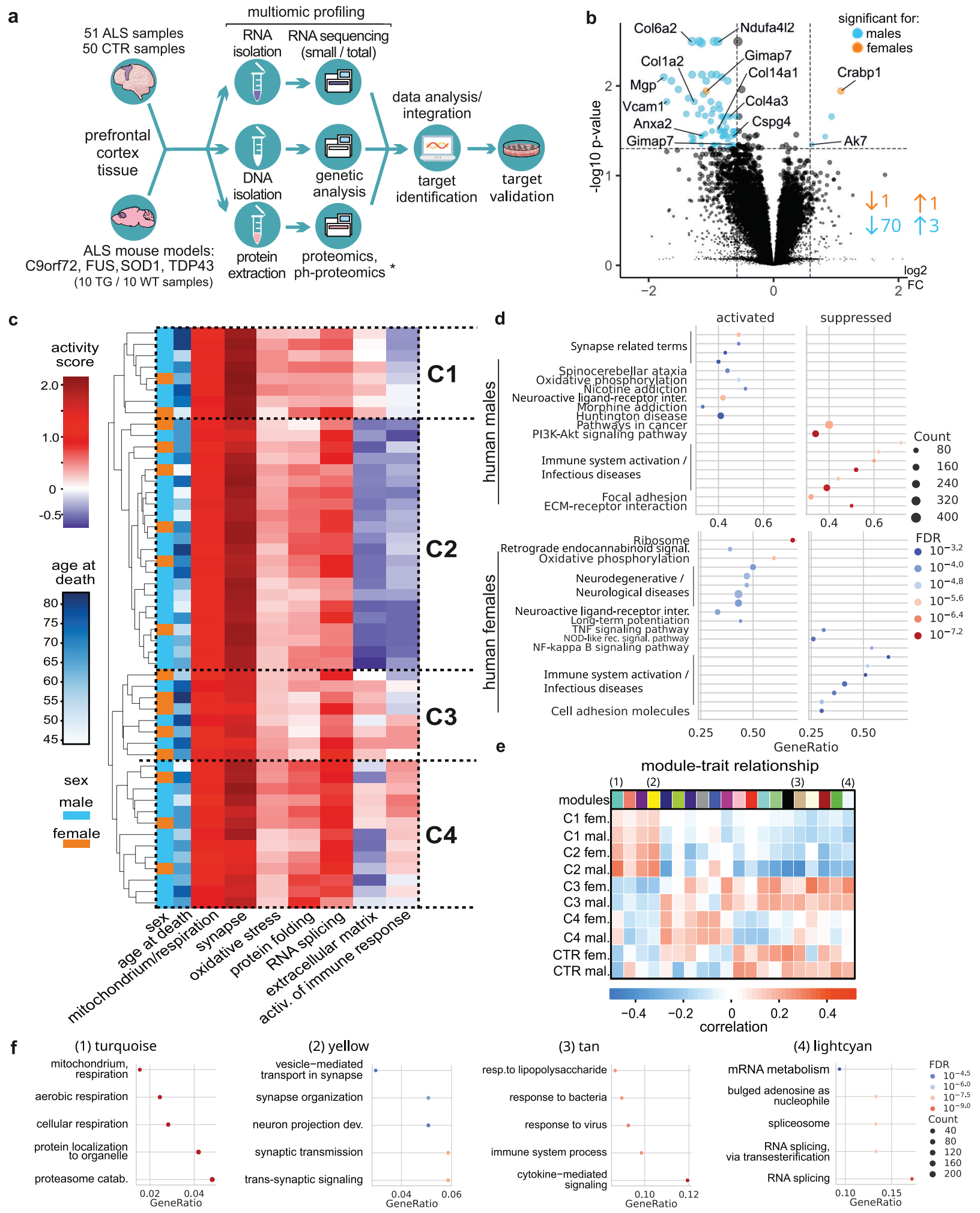
a
multiomic profiling
51 ALS samples
50 CTR samples
RNA isolation
RNA sequencing (small / total)
prefrontal cortex tissue
DNA isolation
genetic analysis
data analysis/ integration
target identification
target validation
ALS mouse models: C9orf72, FUS, SOD1, TDP43
(10 TG / 10 WT samples)
protein extraction
proteomics, ph-proteomics *
b
significant for:
males
females
Col6a2
Ndufa4l2
Gimap7
Col1a2
Col14a1
Crabp1
Mgp
Vcam1
Col4a3
Anxa2
Cspg4
Gimap7
Ak7
-log10 p-value
log2 FC
↓1 ↑1
↓70 ↑3
c
activity score
age at death
sex
male
female
C1
C2
C3
C4
sex
age at death
mitochondrium/respiration
synapse
oxidative stress
protein folding
RNA splicing
extracellular matrix
activ. of immune response
d
activated
suppressed
human males
human females
Synapse related terms
Spinocerebellar ataxia
Oxidative phosphorylation
Nicotine addiction
Neuroactive ligand-receptor inter.
Morphine addiction
Huntington disease
Pathways in cancer
PI3K-Akt signaling pathway
Immune system activation / Infectious diseases
Focal adhesion
ECM-receptor interaction
Ribosome
Retrograde endocannabinoid signal.
Oxidative phosphorylation
Neurodegenerative / Neurological diseases
Neuroactive ligand-receptor inter.
Long-term potentiation
TNF signaling pathway
NOD-like rec. signal. pathway
NF-kappa B signaling pathway
Immune system activation / Infectious diseases
Cell adhesion molecules
GeneRatio
Count
FDR
e
module-trait relationship
modules
C1 fem.
C1 mal.
C2 fem.
C2 mal.
C3 fem.
C3 mal.
C4 fem.
C4 mal.
CTR fem.
CTR mal.
correlation
f
(1) turquoise
mitochondrium, respiration
aerobic respiration
cellular respiration
protein localization to organelle
proteasome catab.
(2) yellow
vesicle−mediated transport in synapse
synapse organization
neuron projection dev.
synaptic transmission
trans-synaptic signaling
(3) tan
resp.to lipopolysaccharide
response to bacteria
response to virus
immune system process
cytokine−mediated signaling
(4) lightcyan
mRNA metabolism
bulged adenosine as nucleophile
spliceosome
RNA splicing, via transesterification
RNA splicing
GeneRatio
FDR
Count

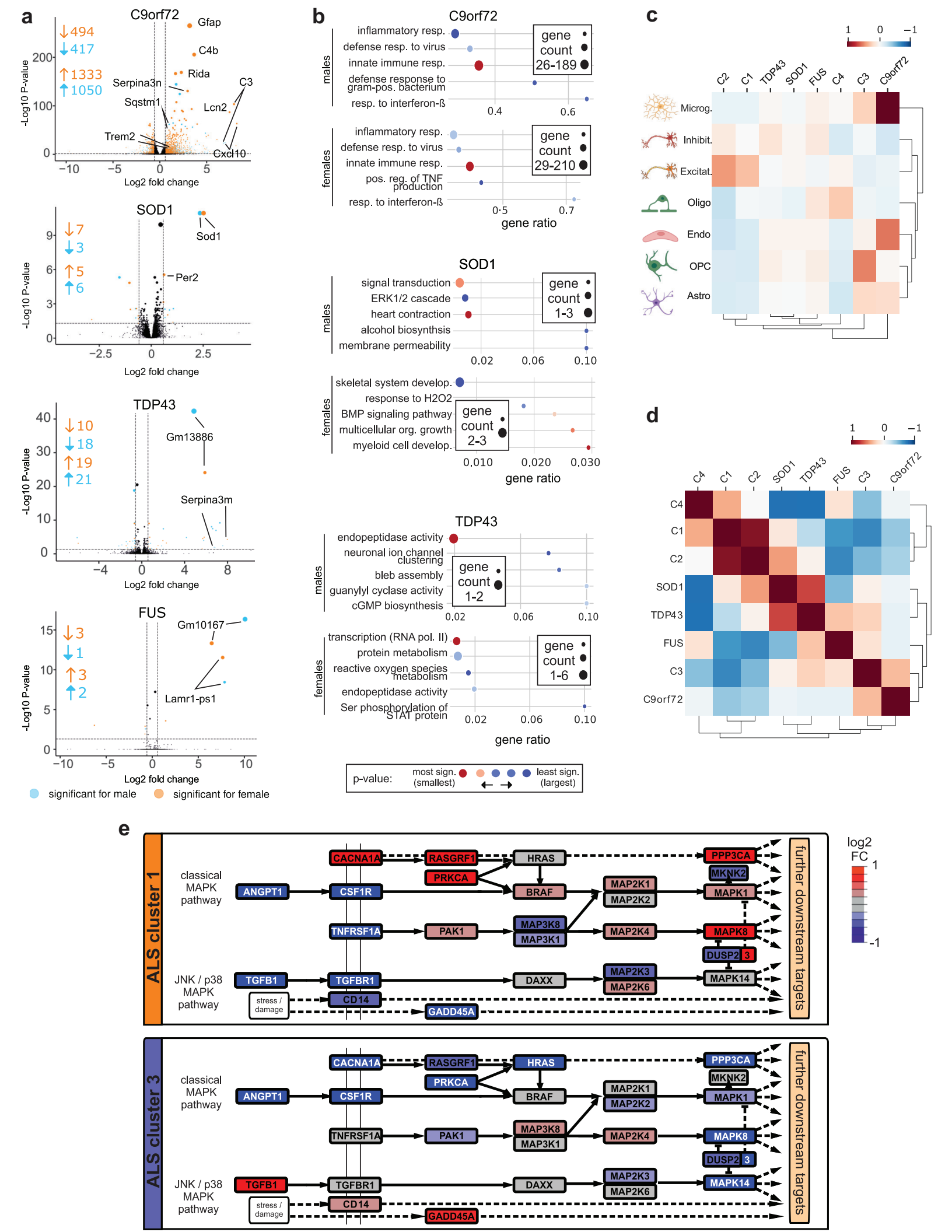
a
C9orf72
↓494
↓417
↑1333
↑1050
Gfap
C4b
Rida
Serpina3n
C3
Sqstm1
Lcn2
Trem2
Cxcl10
-Log10 P-value
Log2 fold change
SOD1
↓7
↓3
↑5
↑6
Sod1
Per2
TDP43
↓10
↓18
↑19
↑21
Gm13886
Serpina3m
FUS
↓3
↓1
↑3
↑2
Gm10167
Lamr1-ps1
significant for male
significant for female
b
C9orf72
males
inflammatory resp.
defense resp. to virus
innate immune resp.
defense response to gram-pos. bacterium
resp. to interferon-ß
gene count 26-189
females
inflammatory resp.
defense resp. to virus
innate immune resp.
pos. reg. of TNF production
resp. to interferon-ß
gene count 29-210
gene ratio
SOD1
males
signal transduction
ERK1/2 cascade
heart contraction
alcohol biosynthsis
membrane permeability
gene count 1-3
females
skeletal system develop.
response to H2O2
BMP signaling pathway
multicellular org. growth
myeloid cell develop.
gene count 2-3
gene ratio
TDP43
males
endopeptidase activity
neuronal ion channel clustering
bleb assembly
guanylyl cyclase activity
cGMP biosynthesis
gene count 1-2
females
transcription (RNA pol. II)
protein metabolism
reactive oxygen species metabolism
endopeptidase activity
Ser phosphorylation of STAT protein
gene count 1-6
gene ratio
p-value:
most sign. (smallest)
least sign. (largest)
c
C2
C1
TDP43
SOD1
FUS
C4
C3
C9orf72
Microg.
Inhibit.
Excitat.
Oligo
Endo
OPC
Astro
d
C4
C1
C2
SOD1
TDP43
FUS
C3
C9orf72
e
ALS cluster 1
classical MAPK pathway
JNK / p38 MAPK pathway
ANGPT1
CSF1R
TNFRSF1A
TGFB1
TGFBR1
stress / damage
CD14
GADD45A
CACNA1A
RASGRF1
PRKCA
HRAS
BRAF
PAK1
MAP3K8
MAP3K1
DAXX
MAP2K1
MAP2K2
MAP2K4
MAP2K3
MAP2K6
PPP3CA
MKNK2
MAPK1
MAPK8
DUSP2
3
MAPK14
further downstream targets
log2 FC
ALS cluster 3

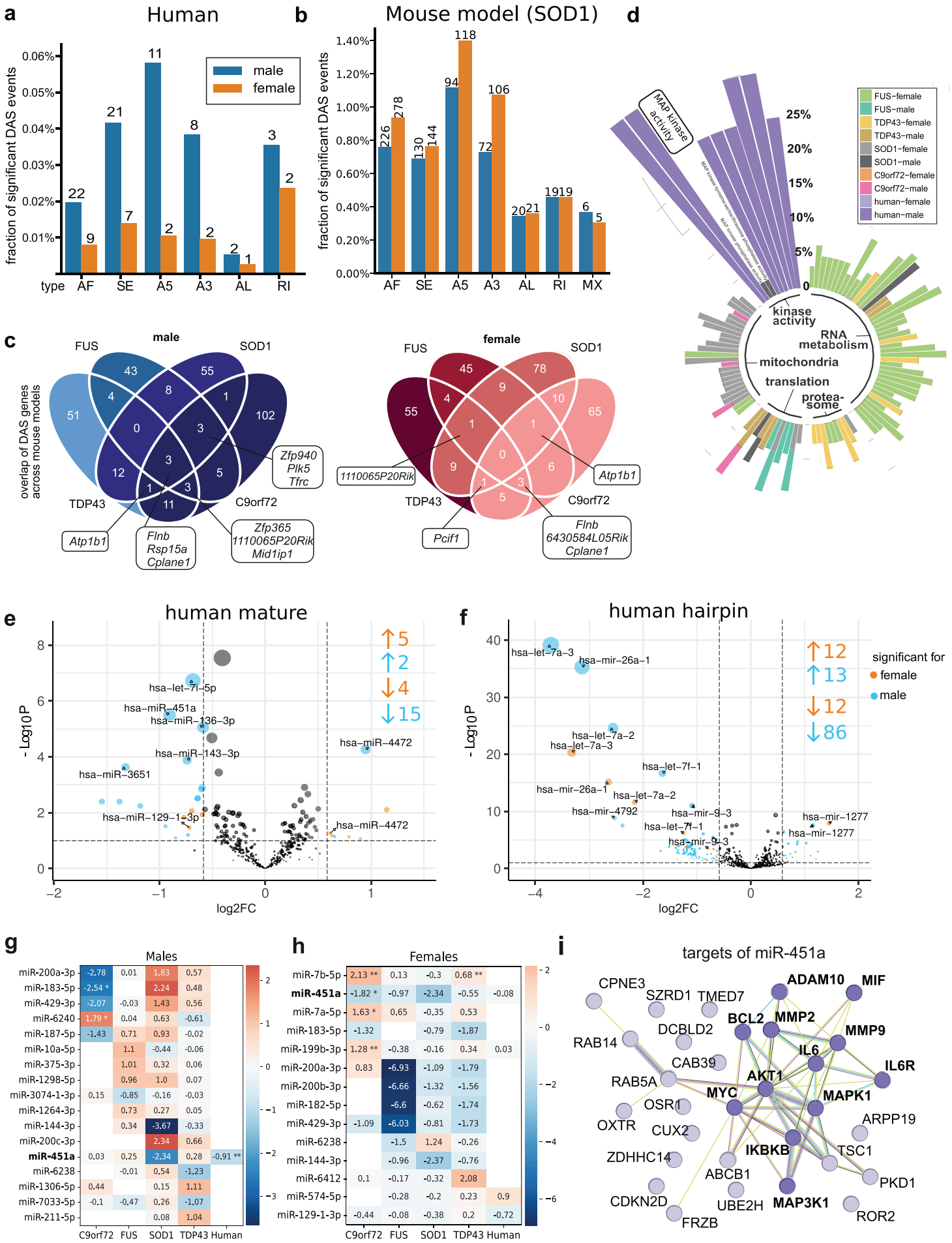
a
Human
fraction of significant DAS events
0.06%
0.05%
0.04%
0.03%
0.02%
0.01%
male
female
22
9
21
7
11
2
8
2
2
1
3
2
type
AF
SE
A5
A3
AL
RI
b
Mouse model (SOD1)
fraction of significant DAS events
1.40%
1.20%
1.00%
0.80%
0.60%
0.40%
0.20%
0.00%
226
278
130
144
94
118
72
106
20
21
19
19
6
5
AF
SE
A5
A3
AL
RI
MX
d
MAP kinase activity
25%
20%
15%
10%
5%
0
FUS−female
FUS−male
TDP43−female
TDP43−male
SOD1−female
SOD1−male
C9orf72−female
C9orf72−male
human−female
human−male
kinase activity
RNA metabolism
mitochondria
translation
protea-some
c
male
FUS
SOD1
TDP43
C9orf72
overlap of DAS genes across mouse models
43
55
4
8
1
51
0
3
102
12
3
5
1
3
11
Zfp940
Plk5
Tfrc
Atp1b1
Flnb
Rsp15a
Cplane1
Zfp365
1110065P20Rik
Mid1ip1
female
FUS
SOD1
TDP43
C9orf72
45
78
9
4
10
55
1
1
65
9
0
6
1
3
5
1110065P20Rik
Atp1b1
Pcif1
Flnb
6430584L05Rik
Cplane1
e
human mature
- Log10P
log2FC
↑5
↑2
↓4
↓15
hsa−let−7i−5p
hsa−miR−451a
hsa−miR−136−3p
hsa−miR−143−3p
hsa−miR−3651
hsa−miR−129−1−3p
hsa−miR−4472
hsa−miR−4472
f
human hairpin
- Log10P
log2FC
↑12
↑13
↓12
↓86
significant for
female
male
hsa−let−7a−3
hsa−mir−26a−1
hsa−let−7a−2
hsa−let−7a−3
hsa−let−7f−1
hsa−mir−26a−1
hsa−let−7a−2
hsa−mir−4792
hsa−mir−9−3
hsa−let−7f−1
hsa−mir−9−3
hsa−mir−1277
hsa−mir−1277
g
Males
miR-200a-3p -2.78 0.01 1.83 0.57
miR-183-5p -2.54 * 2.24 0.48
miR-429-3p -2.07 -0.03 1.43 0.56
miR-6240 1.79 * 0.04 0.63 -0.61
miR-187-5p -1.43 0.71 0.93 -0.02
miR-10a-5p 1.1 -0.44 -0.06
miR-375-3p 1.01 0.32 0.06
miR-1298-5p 0.96 1.0 0.07
miR-3074-1-3p 0.15 -0.85 -0.16 -0.03
miR-1264-3p 0.73 0.27 0.05
miR-144-3p 0.34 -3.67 -0.33
miR-200c-3p 2.34 0.66
miR-451a 0.03 0.25 -2.34 0.28 -0.91 **
miR-6238 -0.01 0.54 -1.23
miR-1306-5p 0.44 0.15 1.11
miR-7033-5p -0.1 -0.47 0.26 -1.07
miR-211-5p 0.08 1.04
C9orf72 FUS SOD1 TDP43 Human
h
Females
miR-7b-5p 2.13 ** 0.13 -0.3 0.68 **
miR-451a -1.82 * -0.97 -2.34 -0.55 -0.08
miR-7a-5p 1.63 * 0.65 -0.35 0.53
miR-183-5p -1.32 -0.79 -1.87
miR-199b-3p 1.28 ** -0.38 -0.16 0.34 0.03
miR-200a-3p 0.83 -6.93 -1.09 -1.79
miR-200b-3p -6.66 -1.32 -1.56
miR-182-5p -6.6 -0.62 -1.74
miR-429-3p -1.09 -6.03 -0.81 -1.73
miR-6238 -1.5 1.24 -0.26
miR-144-3p -0.96 -2.37 -0.76
miR-6412 0.1 -0.17 -0.32 2.08
miR-574-5p -0.28 -0.2 0.23 0.9
miR-129-1-3p -0.44 -0.08 -0.38 0.2 -0.72
C9orf72 FUS SOD1 TDP43 Human
i
targets of miR-451a
CPNE3
SZRD1
TMED7
ADAM10
MIF
BCL2
MMP2
MMP9
DCBLD2
RAB14
IL6
IL6R
CAB39
RAB5A
AKT1
MYC
MAPK1
OSR1
ARPP19
OXTR
CUX2
IKBKB
TSC1
ZDHHC14
ABCB1
PKD1
CDKN2D
UBE2H
MAP3K1
ROR2
FRZB

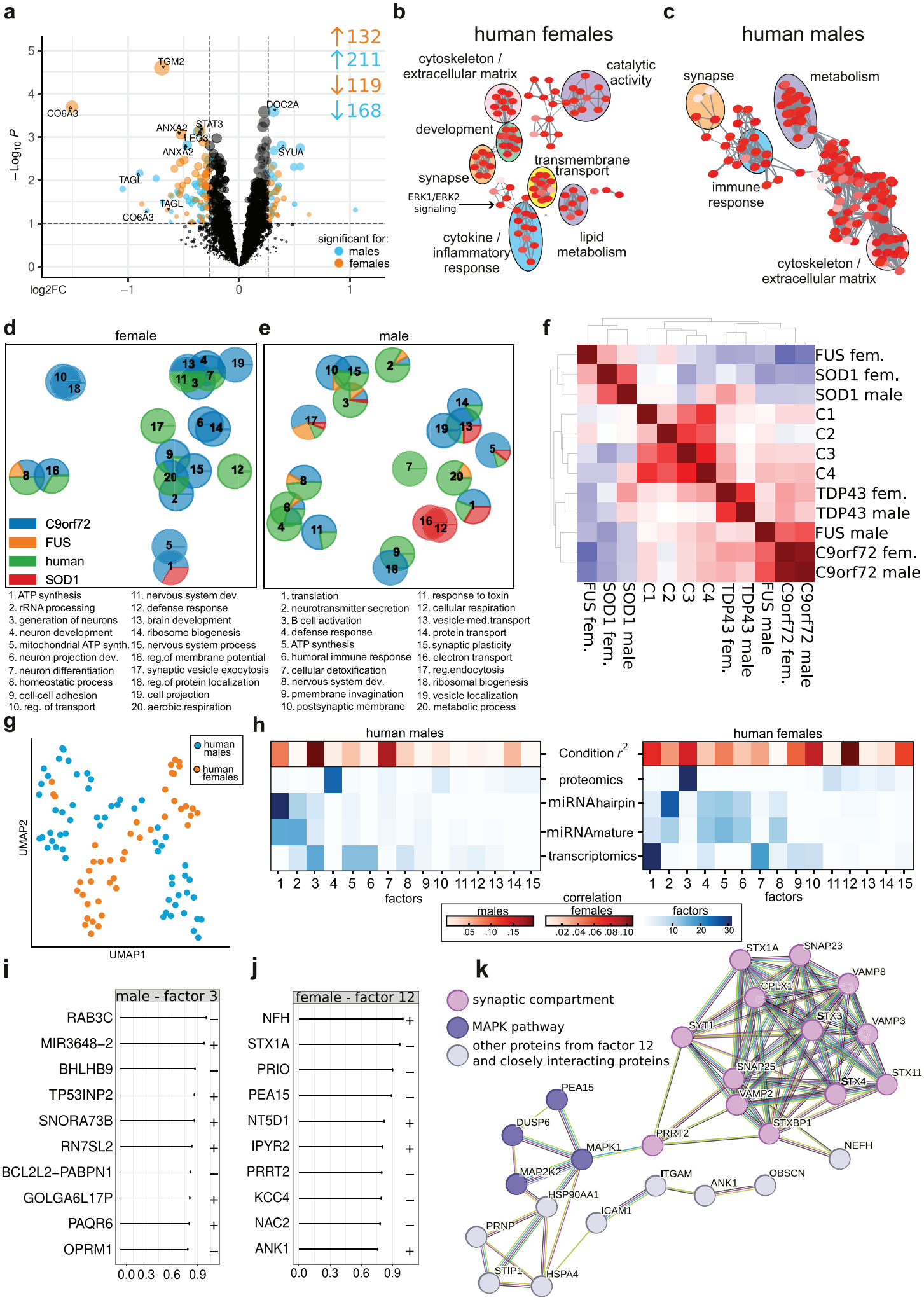
a
↑132
↑211
↓119
↓168
TGM2
CO6A3
DOC2A
ANXA2
STAT3
LEG3
ANXA2
SYUA
TAGL
TAGL
CO6A3
significant for:
males
females
−Log10 P
log2FC
b
human females
cytoskeleton / extracellular matrix
catalytic activity
development
synapse
transmembrane transport
ERK1/ERK2 signaling
cytokine / inflammatory response
lipid metabolism
c
human males
synapse
metabolism
immune response
cytoskeleton / extracellular matrix
d
female
C9orf72
FUS
human
SOD1
1. ATP synthesis
2. rRNA processing
3. generation of neurons
4. neuron development
5. mitochondrial ATP synth.
6. neuron projection dev.
7. neuron differentiation
8. homeostatic process
9. cell-cell adhesion
10. reg. of transport
11. nervous system dev.
12. defense response
13. brain development
14. ribosome biogenesis
15. nervous system process
16. reg.of membrane potential
17. synaptic vesicle exocytosis
18. reg.of protein localization
19. cell projection
20. aerobic respiration
e
male
1. translation
2. neurotransmitter secretion
3. B cell activation
4. defense response
5. ATP synthesis
6. humoral immune response
7. cellular detoxification
8. nervous system dev.
9. pmembrane invagination
10. postsynaptic membrane
11. response to toxin
12. cellular respiration
13. vesicle-med.transport
14. protein transport
15. synaptic plasticity
16. electron transport
17. reg.endocytosis
18. ribosomal biogenesis
19. vesicle localization
20. metabolic process
f
FUS fem.
SOD1 fem.
SOD1 male
C1
C2
C3
C4
TDP43 fem.
TDP43 male
FUS male
C9orf72 fem.
C9orf72 male
g
human males
human females
UMAP2
UMAP1
h
human males
human females
Condition r^2
proteomics
miRNAhairpin
miRNAmature
transcriptomics
factors
correlation
males
females
factors
i
male - factor 3
RAB3C
MIR3648−2
BHLHB9
TP53INP2
SNORA73B
RN7SL2
BCL2L2−PABPN1
GOLGA6L17P
PAQR6
OPRM1
j
female - factor 12
NFH
STX1A
PRIO
PEA15
NT5D1
IPYR2
PRRT2
KCC4
NAC2
ANK1
k
synaptic compartment
MAPK pathway
other proteins from factor 12 and closely interacting proteins
STX1A
SNAP23
VAMP8
CPLX1
SYT1
STX3
VAMP3
SNAP25
STX4
STX11
VAMP2
STXBP1
NEFH
PEA15
DUSP6
MAPK1
PRRT2
MAP2K2
HSP90AA1
ITGAM
ANK1
OBSCN
ICAM1
PRNP
STIP1
HSPA4

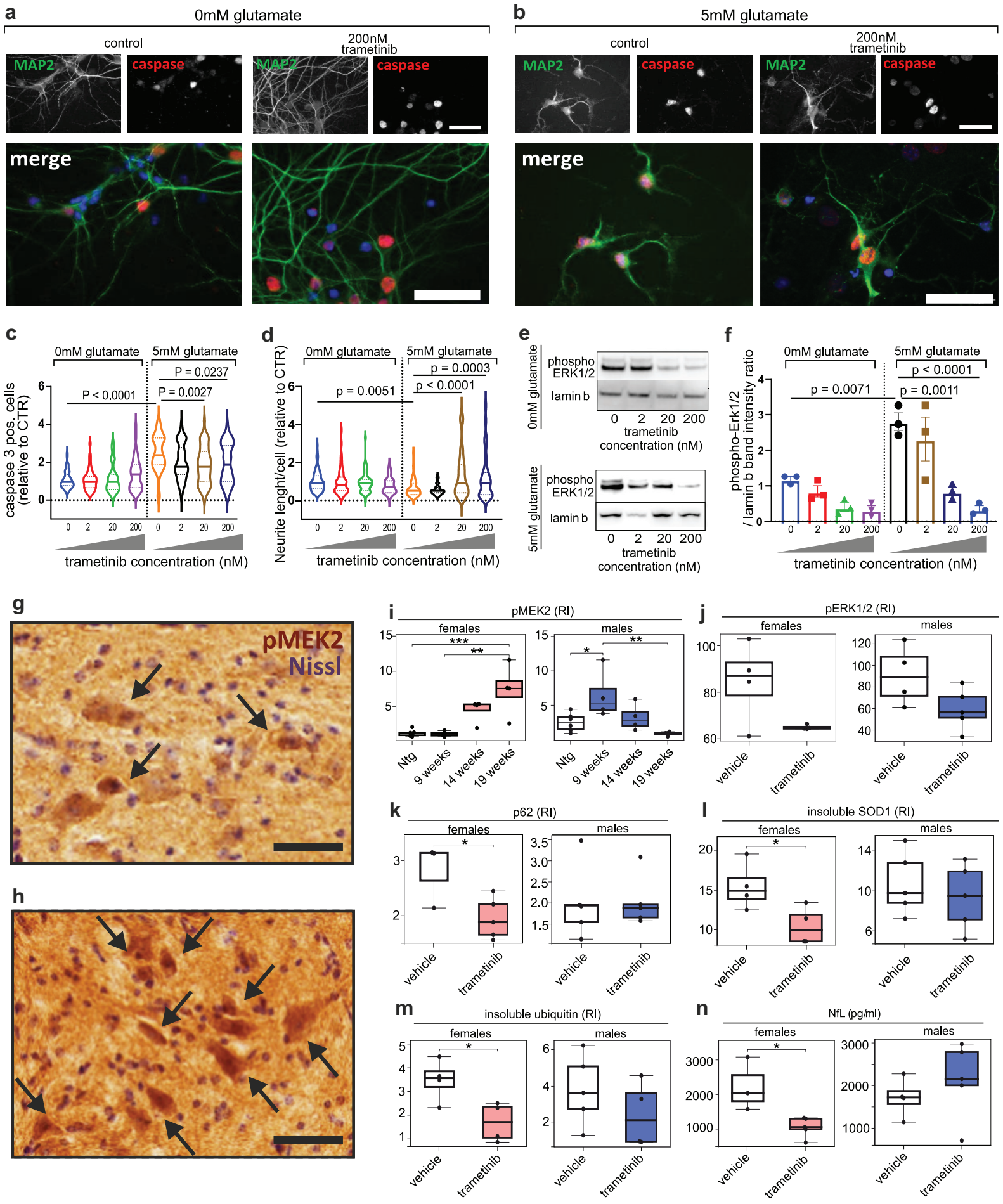
a
0mM glutamate
control
200nM trametinib
MAP2
caspase
merge
b
5mM glutamate
control
200nM trametinib
MAP2
caspase
merge
c
0mM glutamate
5mM glutamate
P < 0.0001
P = 0.0237
P = 0.0027
caspase 3 pos. cells (relative to CTR)
trametinib concentration (nM)
d
0mM glutamate
5mM glutamate
p = 0.0051
p = 0.0003
p < 0.0001
Neurite lenght/cell (relative to CTR)
trametinib concentration (nM)
e
0mM glutamate
phospho ERK1/2
lamin b
trametinib concentration (nM)
5mM glutamate
phospho ERK1/2
lamin b
trametinib concentration (nM)
f
0mM glutamate
5mM glutamate
p = 0.0071
p < 0.0001
p = 0.0011
phospho-Erk1/2 / lamin b band intensity ratio
trametinib concentration (nM)
g
pMEK2
Nissl
h
i
pMEK2 (RI)
females
males
Ntg
9 weeks
14 weeks
19 weeks
j
pERK1/2 (RI)
females
males
vehicle
trametinib
k
p62 (RI)
females
males
vehicle
trametinib
l
insoluble SOD1 (RI)
females
males
vehicle
trametinib
m
insoluble ubiquitin (RI)
females
males
vehicle
trametinib
n
NfL (pg/ml)
females
males
vehicle
trametinib